Spectral Retrieval of Latent Heating Profiles from TRMM PR Data. Part III: Estimating Apparent Moisture Sink Profiles over Tropical Oceans

SHOICHI SHIGE

Department of Aerospace Engineering, Osaka Prefecture University, Osaka, Japan

YUKARI N. TAKAYABU

Center for Climate System Research, University of Tokyo, Chiba, and Institute of Observational Research for Global Change, Japan Agency for Marine-Earth Science and Technology, Kanagawa, Japan

WEI-KUO TAO

Laboratory for Atmospheres, NASA Goddard Space Flight Center, Greenbelt, Maryland

(Manuscript received 19 March 2007, in final form 20 August 2007)

ABSTRACT

The spectral latent heating (SLH) algorithm was developed to estimate apparent heat source (Q_1) profiles for the Tropical Rainfall Measuring Mission (TRMM) precipitation radar (PR) in Parts I and II of this study. In this paper, the SLH algorithm is used to estimate apparent moisture sink (Q_2) profiles. The procedure of Q_2 retrieval is the same as that of heating retrieval except for using the Q_2 profile lookup tables derived from numerical simulations of tropical cloud systems from the Tropical Ocean and Global Atmosphere (TOGA) Coupled Ocean–Atmosphere Response Experiment (COARE) utilizing a cloud-resolving model (CRM). The Q_2 profiles were reconstructed from CRM-simulated parameters with the COARE table and then compared with CRM-simulated "true" Q_2 profiles, which were computed directly from the water vapor equation in the model. The consistency check indicates that discrepancies between the SLH-reconstructed and CRM-simulated profiles for Q_2, especially at low levels, are larger than those for Q_1 and are attributable to moistening for the nonprecipitating region that SLH cannot reconstruct. Nevertheless, the SLH-reconstructed total Q_2 profiles are in good agreement with the CRM-simulated ones. The SLH algorithm was applied to PR data, and the results were compared with Q_2 profiles derived from the budget study. Although discrepancies between the SLH-retrieved and sounding-based profiles for Q_2 for the South China Sea Monsoon Experiment (SCSMEX) are larger than those for heating, key features of the vertical profiles agree well. The SLH algorithm can also estimate differences of Q_2 between the western Pacific Ocean and the Atlantic Ocean, consistent with the results from the budget study.

1. Introduction

The Tropical Rainfall Measuring Mission (TRMM; Simpson et al. 1988, 1996; Kummerow et al. 2000), a joint Japanese–U.S. cooperative earth probe satellite, was successfully launched in 1997 to advance understanding of the global energy and water cycle. The TRMM precipitation radar (PR) is the first spaceborne precipitation radar and can provide height information based upon the time delay of the precipitation-backscattered return power (Kozu et al. 2001; Okamoto 2003). This allows vertical profiles of precipitation to be obtained directly over the global Tropics (Iguchi and Meneghini 1994; Iguchi et al. 2000; Iguchi 2007). The high vertical resolution (250 m at nadir) and quasi-vertical beam of the PR allow it to identify a bright band for a higher percentage of all echoes than can a quasi–horizontally scanning ground radar. Therefore, the classification between convective and stratiform regions of mesoscale convective systems (MCS) has become more straightforward when utilizing the presence of the bright band (Awaka et al. 1998, 2007).

Takayabu (2002) obtained a spectral expression of

Corresponding author address: Dr. Shoichi Shige, Department of Aerospace Engineering, Osaka Prefecture University, 1-1 Gakuen-cho, Sakai, Osaka 599-8531, Japan.
E-mail: shige@aero.osakafu-u.ac.jp

DOI: 10.1175/2007JAMC1738.1

precipitation profiles to examine convective and stratiform rain characteristics as a function of precipitation-top height (PTH) over the equatorial area observed by the TRMM PR. Based on the results of the spectral precipitation statistics of Takayabu (2002), the spectral latent heating (SLH) algorithm was developed for the TRMM PR in Shige et al. (2004, hereinafter Part I). This method uses PR information (i.e., PTH, precipitation rates at the surface and melting level, and convective/stratiform classification) to select the heating profiles in lookup tables. Heating-profile lookup tables for the three rain types—convective, shallow stratiform, and anvil rain (deep stratiform with a PTH higher than the melting level)—were derived with numerical simulations of tropical cloud systems in the Tropical Ocean and Global Atmosphere Coupled Ocean–Atmosphere Response Experiment (TOGA COARE; Webster and Lukas 1992), utilizing a cloud-resolving model (CRM). For convective and shallow stratiform regions, the lookup table is based on the PTH. Considering the sensitivity of the PR, we used a threshold of 0.3 mm h^{-1} to determine the PTH. Properties (i.e., shape and magnitude) of the convective and shallow stratiform heating profiles show near-monotonic change with PTH, suggesting that the distribution of latent heating is a strong function of PTH. On the other hand, the PR cannot observe the PTH accurately enough for the anvil regions because of its insensitivity to the small ice-phase hydrometeors (Heymsfield et al. 2000). The anvil heating profile is much more uniform than the convective heating profile in the tropical convective systems, such that the height of maximum anvil heating is not overly sensitive to storm-height observation. Thus, for the anvil region, the lookup table refers to the precipitation rate at the melting level P_m instead of PTH. Houze et al. (1980), Gamache and Houze (1983), and Chong and Hauser (1989) showed that the stratiform precipitation falling into the melting layer from the anvil cloud above is a combination of condensate generated in and carried over from the convective region plus condensate that is produced by the anvil region's own upward motion, analyzing the water budgets of a precipitating tropical mesoscale convective system. The contribution by the horizontal transfer of condensate from the convective region to the anvil region is included in the lookup tables (Fig. 7 of Part I).

In a subsequent paper (Shige et al. 2007, hereinafter Part II), the universality of the lookup table produced from COARE simulations used in the SLH algorithm was examined for its global application to TRMM PR data and improvements were made to the SLH algorithm. In the revised procedure for convective heating retrieval, the upper-level heating amplitude due to ice processes and lower-level heating amplitude due to liquid water processes are determined separately. Braun and Houze (1995) showed that the peak heating rate by freezing within the convective region occurs immediately above the freezing level. Based on sensitivity tests, the level separating upper-level heating from lower-level heating is determined to be 1 km above the melting level. The upper-level heating due to ice processes is determined by P_f, where P_f is the precipitation rate at the level separating upper-level heating from lower-level heating. The lower-level heating due to liquid water processes is determined by P_s, where P_s is the precipitation rate at the lowest observable level. In the stratiform region, the heating profile is shifted up or down by matching the melting level in the COARE lookup table with the observed one. The revised SLH algorithm was applied to PR data, and the results were compared with Q_1 profiles that were derived diagnostically from the 1998 South China Sea Monsoon Experiment (SCSMEX; Lau et al. 2000) Northern Enhanced Sounding Array (NESA) sounding data (Johnson and Ciesielski 2002), where Q_1 is the apparent heat source budget defined in Yanai et al. (1973). Key features of the vertical profiles agree well—in particular, the level of maximum heating. Differences of heating profiles between the western Pacific Ocean (more "top heavy") and the Atlantic Ocean (more "bottom heavy") estimated by the SLH algorithm are also consistent with those from the budget study (Thompson et al. 1979; see a review by Cotton and Anthes 1989). Utilizing the information on precipitation profiles, the SLH algorithm retrieves differences in the shape of the convective heating profile between the eastern and western Pacific during the cold phase. The differences in the shape of convective heating profiles across the Pacific are consistent with the results from reanalysis datasets (Back and Bretherton 2006).

Large-scale models (i.e., general circulation and climate models) require not only the vertical distribution of Q_1, but also that of Q_2, where Q_2 is the apparent moisture sink budget defined in Yanai et al. (1973). Rajendran et al. (2004) developed a new empirical cumulus parameterization scheme (ECPS), based on a procedure to improve the vertical distribution of heating and drying over the Tropics. The ECPS utilizes observed profiles of Q_1 derived using the TRMM Microwave Imager (TMI) convective–stratiform heating algorithm (Tao et al. 1993) and the European Centre for Medium-Range Weather Forecasts analysis-based Q_2. Comparisons between short-range ECPS forecasts and those made with the modified Kuo scheme (Krishnamurti et al. 1983) show a marked improvement in the skill in the ECPS. More improvements may be achieved

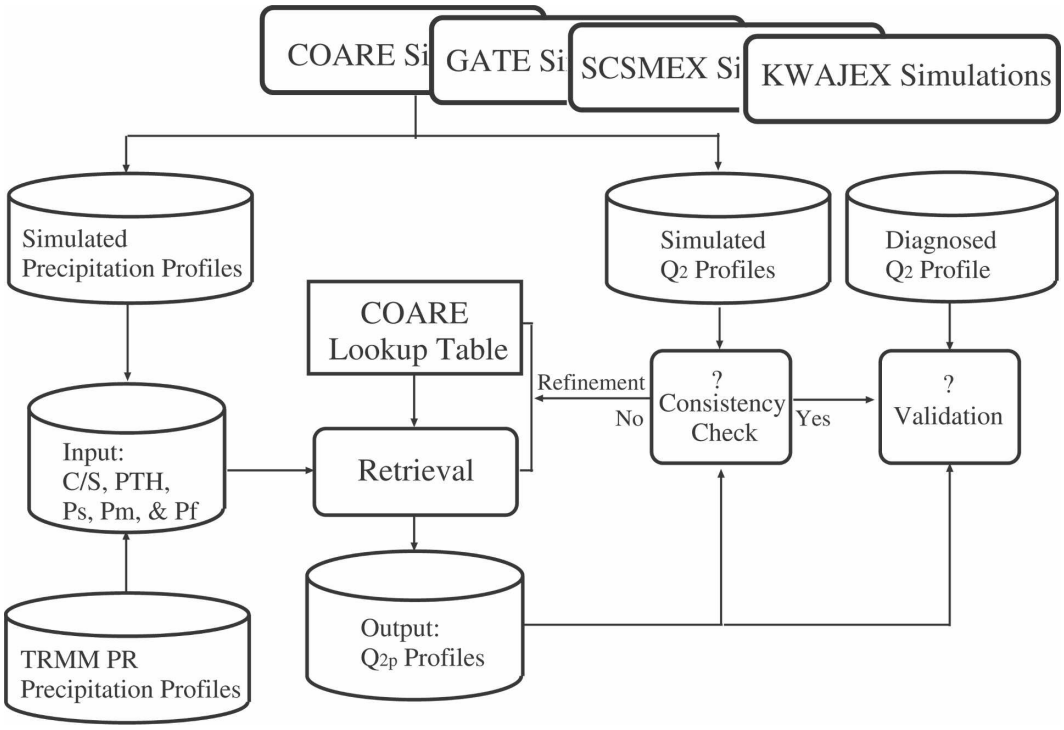

FIG. 1. Diagram showing the procedure for refining and validating the Q_2 profile retrieval using the SLH algorithm. Letters denote convective and stratiform classification (C/S), PTH, the precipitation rate P_s at the lowest observable level, the precipitation rate P_m at the melting level, the precipitation rate P_f at the level separating upper-level heating from lower-level heating, and Q_2 mainly due to precipitation processes (Q_{2p}). The "?" refers to a comparison and examination of the Q_{2p} profiles reconstructed from the SLH algorithm with the Q_2 profiles from model simulations. This consistency check is a necessary precondition for the application of the algorithm to actual TRMM PR data.

with the ECPS utilizing both Q_1 and Q_2 profiles derived from TRMM data (J. Rajendran 2005, personal communication). However, none of the TRMM heating algorithms estimate Q_2 profiles (see a review by Tao et al. 2006).

In addition to improving large-scale model simulations, physical insights into convection can be gained by having both Q_1 and Q_2 profiles. By combining the Q_1 and Q_2 equations, one can examine the eddy fluxes that have been widely used to measure the intensity of convection (e.g., Ninomiya 1968, 1971; Nitta 1972, 1975, 1977; Yanai et al. 1973, 1976; Johnson 1976; Gallus and Johnson 1991). Careful comparison between the vertical distributions of Q_1 and Q_2 yields valuable information on the nature of heating processes (e.g., Nitta and Esbensen 1974; Luo and Yanai 1984; Johnson and Lin 1997). For example, coincident peaks indicate mostly stratiform rainfall, whereas widely separated peaks indicate strong eddy fluxes or an important contribution by deep convection.

In this study, the SLH algorithm is used to estimate the Q_2 profile. First, differences between Q_1 and Q_2 are examined. Second, Q_2 profiles are reconstructed from CRM-simulated parameters (i.e., convective/stratiform classification, PTH, P_s, P_m, and P_f) and are compared with the "true" CRM-simulated Q_2 profiles, which are computed directly by the water vapor equation in the model. Third, the SLH algorithm is applied to PR data and the results are compared with Q_2 profiles derived diagnostically from SCSMEX sounding data (Johnson and Ciesielski 2002). It is also applied to PR data for February 1998 and February 1999 to highlight the differences between El Niño and La Niña events.

2. Approach

Figure 1 shows the procedure for refining and validating the Q_2 profile retrieval using the SLH algorithm. Because of the scarcity of reliable validation data and difficulties associated with the collocation of validation data and satellite measurements, a consistency check of the SLH algorithm is performed using CRM-simulated precipitation profiles as a proxy for the PR data. The SLH algorithm estimates Q_2 that is mainly due to pre-

cipitation processes, because it is severely limited by the inherent sensitivity of the PR, which can detect only precipitation-sized particles. Hereinafter, Q_2 estimated by the SLH algorithm is represented as Q_{2p} to bring attention to this point. Algorithm-reconstructed Q_{2p} profiles are derived from CRM-simulated precipitation profiles and are compared with CRM-simulated true Q_2 profiles, which are computed directly from the water vapor equation in the model. The consistency check is a useful and necessary precondition for the application of the algorithm to actual TRMM PR data. CRM-simulated data from TOGA COARE, the Global Atmospheric Research Program Atlantic Tropical Experiment (GATE; Houze and Betts 1981), SCSMEX NESA, and the 1999 Kwajelin Atoll Field Experiment (KWAJEX; Yuter et al. 2005) are used as a consistency check. Locations of sounding arrays deployed for TOGA COARE, GATE, SCSMEX NESA, and KWAJEX are shown in Fig. 2 of Part II. Only precipitation over ocean is considered in the current investigation. Significant differences in precipitation features between ocean and land have been shown by TRMM observations (e.g., Nesbitt et al. 2000; Petersen and Rutledge 2001; Takayabu 2002, 2006; Schumacher and Houze 2003a,b). Continental locations exhibit marked variability in precipitation structure both regionally and seasonally; thus we possibly need to vary the lookup table regionally and seasonally. Simulations of other field experiments [e.g., the Global Energy and Water Cycle Experiment Asian Monsoon Experiment (GAME) in the Indo-China Peninsula (Yasunari 1994) and the Atmospheric Radiation Measurement Program in the southern U.S. Great Plains (Ackerman and Stokes 2003)] are needed to produce lookup tables for precipitation over land but are beyond the scope of this study. For a true test, the SLH algorithm is applied to PR data and the results are compared with Q_2 profiles derived diagnostically from SCSMEX NESA sounding data (Johnson and Ciesielski 2002) in this paper.

The CRM used in this study is the two-dimensional version of the Goddard Cumulus Ensemble (GCE) model (Tao and Simpson 1993; Tao et al. 2003). Tropical convective systems in TOGA COARE, GATE, SCSMEX NESA, and KWAJEX are simulated with the so-called cloud ensemble modeling approach, as explained in Part II. Details of model settings were provided in Part II. Note that the TOGA COARE and GATE simulations in this study are not the same as those in Part II. The TOGA COARE and GATE simulations in this study were made with the TOGA COARE flux algorithm (Fairall et al. 1996; Wang et al. 1996) and a modification of the conversion of cloud ice to snow in the ice microphysics schemes (Tao et al. 2003) as well as the SCSMEX and KWAJEX simulations. The accuracy of the convective–stratiform separation affects the determination of the vertical distribution of heating and drying. The TRMM PR rain-type classifications, in which brightband identification is very important, cannot be directly applied to GCE outputs (Awaka et al. 1996). The microphysical schemes utilized in CRMs (e.g., Lin et al. 1983; Rutledge and Hobbs 1984) typically do not contain an explicit description of the partially melted precipitation particles that lead to a bright band of enhanced radar reflectivity. Thus, the GCE convective and stratiform separation method (Lang et al. 2003) is used with some modifications described in Part I to maintain the consistency with the TRMM PR version-6 2A23 convective–stratiform separation algorithm (Awaka et al. 2007). Considering the sensitivity of the PR, we classified model grid points that have a precipitation less than a threshold of 0.3 mm h^{-1} as a nonprecipitating region.

3. Heat and moisture budgets

In diagnostic studies (Yanai et al. 1973; Yanai and Johnson 1993), it is customary to define the apparent heat source Q_1 and the apparent moisture sink Q_2 of a large-scale system by averaging horizontally the thermodynamic and water vapor equations as

$$Q_1 = \overline{\pi}\left(\frac{\partial\overline{\theta}}{\partial t} + \overline{\mathbf{v}}\cdot\nabla\overline{\theta} + \overline{w}\frac{\partial\overline{\theta}}{\partial z}\right) \quad \text{and} \tag{1}$$

$$Q_2 = -\frac{L_v}{C_p}\left(\frac{\partial\overline{q}_v}{\partial t} + \overline{\mathbf{v}}\cdot\nabla\overline{q}_v + \overline{w}\frac{\partial\overline{q}_v}{\partial z}\right), \tag{2}$$

where θ is the potential temperature, q_v is the mixing ratio of water vapor, $\mathbf{v}$ is the horizontal velocity, w is the vertical velocity, $\pi = (p/P_{00})^{R/C_p}$ is the nondimensional pressure, p is the pressure, P_{00} is the reference pressure (1000 hPa), C_p is the specific heat of dry air at constant pressure, R is the gas constant for dry air, L_v is the latent heat of vaporization, z is height, and t is time. The overbars denote horizontal averages.

Both Q_1 and Q_2 can be directly related to the contributions of cloud effects, which can be explicitly estimated by CRMs as

$$Q_1 = \overline{\pi}\left(-\frac{1}{\rho}\frac{\partial\overline{\rho}\,\overline{w'\theta'}}{\partial z} - \overline{\mathbf{v}'\cdot\nabla\theta'} + \overline{D}_\theta\right) + \overline{\mathrm{LH}} + \overline{Q}_R \quad \text{and} \tag{3}$$

$$Q_2 = \frac{L_v}{C_p}\left(\frac{1}{\overline{\rho}}\frac{\partial\overline{\rho}\,\overline{w'q'_v}}{\partial z} - \overline{\mathbf{v}'\cdot\nabla q'_v} + \overline{D}_{q_v}\right) + \overline{\mathrm{NC}}. \tag{4}$$

The primes indicate deviations from the horizontal averages; $\bar{\rho}$ is the air density and Q_R is the cooling/heating rate associated with radiative processes. The subgrid-scale (smaller than the cloud scale) diffusions are represented by D_θ and D_{q_v}, which are usually small relative to other terms above the boundary layer (Soong and Tao 1980). The terms LH and NC are the net latent heating and the net condensation, respectively, due to the phase change of water:

$$\mathrm{LH} = \frac{L_v}{C_p}(c - e) + \frac{L_f}{C_p}(f - m) + \frac{L_s}{C_p}(d - s) \quad \text{and} \quad (5)$$

$$\mathrm{NC} = \frac{L_v}{C_p}(c - e + d - s). \quad (6)$$

The variables L_f and L_s are the latent heats of fusion and sublimation, respectively. Variables c, e, f, m, d, and s stand for the rates of condensation of cloud droplets, evaporation of cloud droplets and raindrops, freezing of cloud droplets and raindrops, melting of ice crystals, snow and graupel, deposition of ice crystals, and sublimation of all ice hydrometeors, respectively. These processes are not directly detectable with remote sensing (or, for that matter, with in situ measurements). Thus, heating and drying retrieval schemes depend heavily on the use of CRM. The first terms on the right-hand side of Eqs. (3) and (4) are the vertical eddy heat and moisture flux convergences from upward and downward cloud-scale motions, respectively. The second terms are the horizontal eddy heat and moisture flux convergences, respectively.

The precipitation falling at a given time is not related to the drying/moistening (heating/cooling) that is occurring at that instant but rather to the accumulated drying/moistening (heating/cooling) that led up to the precipitation over a finite time period. Therefore, Q_1 and Q_2 should be basically integrated over the time periods encompassing the life cycles of cloud processes producing the precipitation. However, it is extremely difficult to tabulate, for example, the effect of individual mesoscale systems. Instead, we here depend on the statistics. In the CRM simulation, as well as in the real world, cloud systems develop and decay. Although instantaneous matching between a certain precipitation profile and a drying/moistening (heating/cooling) profile is an ill-posed concept, statistical tabulation could still be done, if the life cycle of cloud systems is realistically reproduced in the CRM. For example, a shallow convective precipitation profile may be at a developing stage of a mesoscale system with a certain probability A, and may be just an isolated convection with a probability of $1 - A$. The drying/moistening (heating/cooling) associated with the two cases should be different. However, if the CRM reproduces the statistics of rain systems sufficiently well, CRM-based tables can statistically represent an average drying/moistening (heating/cooling) profile for a certain precipitation profile. We accumulate Q_1 and Q_2 over a period of 5 min for each data sampling, because accumulation over long periods is inadequate for growing convective cells (Shige and Satomura 2000, their Fig. 4a) and fast-moving convective systems. Additional sensitivity tests with periods of 1 and 2 min do not alter the Q_2 profile for the total region but indicate that there are more quantitative differences in convective and stratiform components of Q_2 than in those of Q_1. In this study, the two-dimensional version of the GCE model was used. Real clouds and cloud systems are three-dimensional. Grabowski et al. (1998), Donner et al. (1999), and Zeng et al. (2007) found larger temporal variability in a two-dimensional simulation than in a three-dimensional simulation. Thus, the sensitivity of Q_2 in convective and stratiform regions to accumulated time might be smaller in the three-dimensional simulation than in the two-dimensional simulation, but such discussion is beyond the scope of this study. Hereinafter Q_1 and Q_2 accumulated over a period of 5 min for each data sampling are represented as instantaneous Q_1 and Q_2 to maintain consistency with Part I and Part II.

Figures 2a–f show GCE-simulated average profiles of the heat budget [LH, $Q_1 - Q_R$ (hereinafter Q_{1R}) without and with horizontal eddy heat flux] and moisture budget [NC, Q_2 without and with horizontal eddy heat flux] for the TOGA COARE 19–26 December 1992 case. The difference between LH and NC around 4.4 km is large (Figs. 2a,d). The maximum of NC around 4.4 km can be explained by a decrease in the saturation water vapor mixing ratio, which is due to the melting of ice particles (Guichard et al. 1997). It is also evident that the NC magnitudes are smaller than the LH magnitude above 6 km, because freezing is included in LH [Eq. (5)] but not in NC [Eq. (6)].

The profile of Q_{1R} for the total region (Fig. 2b) is close to that of LH for the total region (Fig. 2a), except near the melting level (~4–5 km) and the upper troposphere (~14–16 km). The vertical eddy heat flux convergence near the melting level compensates for the distinct LH cooling due to the melting for the total region (Sui et al. 1994; Shie et al. 2003) while that in the upper troposphere offsets the net radiation because the saturation mixing ratio is low at high altitudes; thereby, condensation heating is no longer vital (Mapes 2001; Shie et al. 2003). On the other hand, the profile of Q_2 for the total region (Fig. 2e) does not follow that of NC for the total region (Fig. 2d) and has a more complicated shape. Gallus and Johnson (1991) also showed

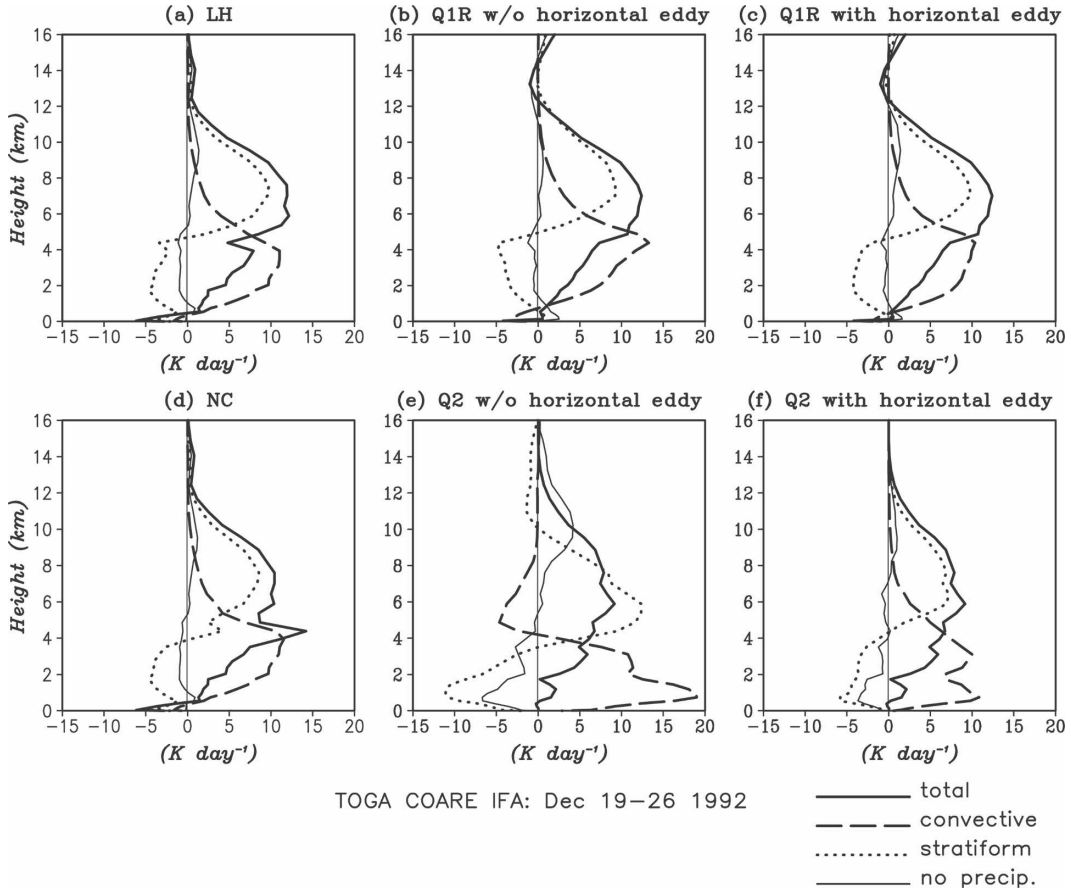

FIG. 2. Eight-day-averaged profiles of the GCE-simulated heat budget [(a) LH, and Q_{1R} (b) without horizontal eddy heat flux and (c) with horizontal eddy heat flux] and moisture budget [(d) NC, and Q_2 (e) without horizontal eddy heat flux and (f) with horizontal eddy heat flux] for the total (thick solid), convective (dashed), stratiform (dotted), and nonprecipitating (thin solid) regions for the TOGA COARE 19–26 Dec 1992 case.

that the profiles of Q_2 associated with a midlatitude squall line are noisier than those of Q_1 using rawinsonde data. The vertical eddy moisture flux convergence is one of the major contributors to Q_2 while the contribution to the Q_{1R} budget by the vertical eddy heat flux convergence is minor, as noted by observations (Chong and Hauser 1990) and modeling studies [Soong and Tao (1980) and many others]. This difference is explained by the fact that the vertical gradient of the mean water vapor is larger than that of the mean potential temperature.

The horizontal eddy heat and moisture flux convergences have been neglected by observational and modeling studies. However, heat and moisture transport from the convective region to the stratiform region may be important because of the embedded mesoscale circulation (i.e., ascending front-to-rear flow and descending rear inflow) within a squall line (Gallus and Johnson 1991). As discussed in Part II, there are differences between profiles of Q_{1R} without and with horizontal eddy heat flux in the convective and stratiform regions—in particular, around the melting level (Figs. 2b,c). Much larger differences between profiles of Q_2 without and with horizontal eddy moisture flux in the convective and stratiform regions are found in Figs. 2e,f. The horizontal eddy moisture flux convergence compensates low-level drying and midtropospheric moistening in the convective regions while compensating low-level moistening and midtropospheric drying in the stratiform regions. The Q_2 profiles with horizontal eddy heat flux in the convective and stratiform regions (Fig. 2f) are similar to the results from Johnson (1984), who partitioned the total Q_2 profile of Yanai et al. (1973) into convective and stratiform components.

Two different mechanisms for the double-peak structure in Q_2 often seen in tropical budget studies (Reed and Recker 1971; Yanai et al. 1973; Johnson 1976) have been proposed: 1) the combined but vertically separated drying effects of convective and stratiform regions (Johnson 1984) and 2) midtropospheric moisten-

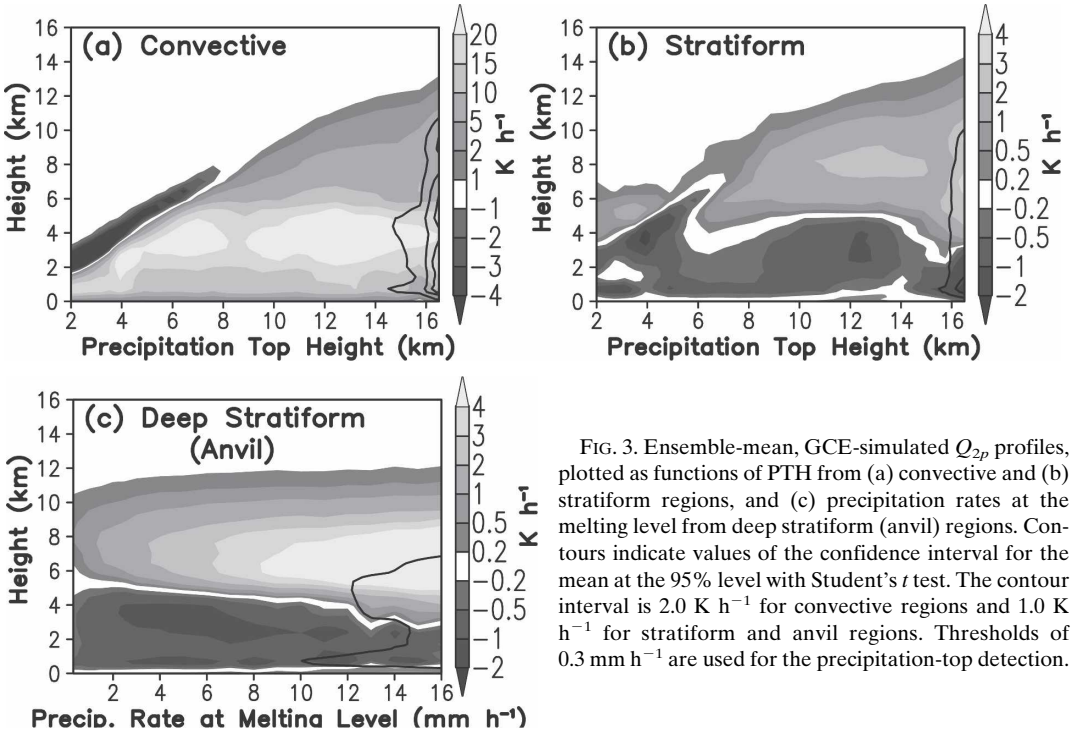

FIG. 3. Ensemble-mean, GCE-simulated Q_{2p} profiles, plotted as functions of PTH from (a) convective and (b) stratiform regions, and (c) precipitation rates at the melting level from deep stratiform (anvil) regions. Contours indicate values of the confidence interval for the mean at the 95% level with Student's t test. The contour interval is 2.0 K h^{-1} for convective regions and 1.0 K h^{-1} for stratiform and anvil regions. Thresholds of 0.3 mm h^{-1} are used for the precipitation-top detection.

ing by vertical eddy moisture convergence in the convective region (Lafore et al. 1988; Caniaux et al. 1994). Lafore et al. (1988) and Caniaux et al. (1994) argued for the latter one based on their numerical simulations of a West African squall line during Convection Profonde Tropicale (COPT)-81. Although the profile of Q_2 in the total region for the TOGA COARE case does not exhibit a prominent double-peak structure, the Q_2 profile without horizontal eddy heat flux in the convective region characterized by midtropospheric moistening (Figs. 2e) is in good agreement with that in the convective region simulated by Caniaux et al. (1994, their Fig. 22b). Lafore et al. (1988) and Caniaux et al. (1994) neglected horizontal eddy moisture flux convergence, as do most previous studies, and thereby may have overestimated the role of the vertical eddy moisture convergence. Lafore et al. (2002) recently simulated a West African system during the Hydrological Atmospheric Pilot Experiment (HAPEX)-Sahel and pointed out the importance of the horizontal eddy flux convergence of heat, moisture, and momentum.

The SLH algorithm estimates Q_{1R} and Q_2 that is mainly due to precipitation processes (Q_{1Rp} and Q_{2p}), because it is severely limited by the inherent sensitivity of the PR that can detect only precipitation-sized particles. It is noticed in Fig. 2 that the Q_2 in the nonprecipitating region is of the same order as that in the stratiform region while the Q_{1R} profile in the nonprecipitating region is negligible. This is consistent with the results from Nitta and Esbensen (1974), which show that moistening rates are about a factor of 3 larger than heating/cooling rates during the undisturbed Barbados Oceanographic and Meteorological Experiment (BOMEX) period in the trade wind belts, attributable to larger contribution of eddy fluxes in Q_2 than in Q_{1R}. Thus, we cannot expect that differences between Q_{2p} and Q_2 are as small as those between Q_{1Rp} and Q_{1R}.

4. Algorithm

a. Construction of lookup tables

The Q_{2p} profile lookup tables have been constructed for the three rain types: convective, shallow stratiform, and deep stratiform, with and without surface rain (Fig. 3). For the construction of lookup tables, the GCE-simulated precipitation profiles and corresponding Q_{2p} profiles from the four subperiods of 9-day duration (10–18 December 1992, 27 December 1992–4 January 1993, 9–17 February 1993, and 18–26 February 1993) are used.

Figure 3a shows the lookup table for convective rain. The GCE-simulated precipitation profiles with a 0.3 mm h^{-1} precipitation-top threshold and corresponding Q_{2p} profiles are accumulated and averaged for each PTH with model grid intervals. Properties (i.e., shape and magnitude) of convective Q_{2p} profiles show less

monotonic changes with PTH than do those of Q_{1Rp} (Part II, their Fig. 5a) because the contribution of eddy fluxes is larger in Q_{2p} than in Q_{1Rp}. The convective Q_{2p} profiles with a PTH lower than 8 km are characterized by moistening around PTH levels resulting from an excess of evaporation over condensation and drying below, such as in trade wind cumulus (Nitta and Esbensen 1974). This feature is consistent with convective heating profiles characterized by cooling aloft (Part II, their Fig. 5a).

As for the stratiform precipitation, the GCE-simulated precipitation profiles with a 0.3 mm h^{-1} precipitation-top threshold and corresponding Q_{2p} profiles are also averaged for each PTH (Fig. 3b). However, as mentioned earlier, we cannot expect the PR to retrieve the small ice-phase precipitation and observe the PTH accurately enough in the upper-level regions of the anvils where small ice-phase hydrometeors dominate. Therefore, only the stratiform Q_{2p} profiles with a PTH lower than 4.4 km (shown in Fig. 3b), characterized by moistening below PTH levels and drying aloft, are used as the shallow stratiform Q_{2p} profile lookup table for the SLH algorithm.

Figure 3c shows a lookup table for anvil (deep stratiform with a PTH higher than the melting level) rain. PR can measure the precipitation rate at the melting level, as can surface-based radar (e.g., Leary and Houze 1979), although it cannot observe the PTH accurately enough in the upper-level regions of the anvils. Thus, for the anvil region, the lookup table refers to the precipitation rate at the melting level P_m instead of PTH (Part I). The anvil profiles with a PTH higher than the melting level are characterized by upper-level drying and lower-level moistening, which is also found in observations (e.g., Johnson and Young 1983). The upper-level drying in these anvil regions is largely due to condensation and deposition, whereas the lower-level moistening is largely due to evaporation of raindrops. The height of the level separating upper-level drying and lower-level moistening decreases with $\tilde{P}_m$, where tildes denote the variables in the lookup table. The cooling around the melting level increases with $\tilde{P}_m$ (see Fig. 7a of Part II). Thus the saturation water vapor mixing ratio decreases, resulting in an increase of NC around the melting level, which accounts for the lowering of the level separating upper-level drying and lower-level moistening. Note that the lookup table for anvil rain does not fully capture the variability in the upper-level drying of the stratiform rain region. Although drying above 12 km is found for the anvil profiles with a PTH higher than 12 km in Fig. 3b, a set maximum height for Q_{2p} profiles can be seen around 12 km in Fig. 3c.

b. Procedure of Q_{2p} retrieval

The procedure for Q_{2p} retrieval is the same as that for heating retrieval (Part II) except for using the Q_{2p} tables (Fig. 3). The SLH algorithm utilizes the observed information on precipitation type (convective or stratiform), PTH, P_s, P_m, and P_f. The convective region is then separated into a shallower convective region and a deeper convective region. On the other hand, the stratiform region is separated into a shallow stratiform region and an anvil region based on the PTH in comparison with the melting level. The algorithm then derives Q_{2p} profiles based on the following procedure for each of the four regions (Fig. 4).

For shallower convective regions (Fig. 4a), as well as shallow stratiform regions (Fig. 4b), a Q_{2p} profile corresponding to the PTH is selected in the convective Q_{2p} profile (Fig. 3a) and PTH-based shallow stratiform Q_{2p} profile (Fig. 3b) lookup tables, respectively. The amplitude is determined by

$$Q(z) = \frac{\tilde{Q}(z)}{\tilde{P}_s} P_s. \tag{7}$$

For deeper convective regions (Fig. 4c), the upper-level drying due to ice processes is determined by

$$Q(z)_{\text{high}} = \frac{\tilde{Q}_{\text{high}}(z)}{\tilde{P}_f} P_f. \tag{8}$$

Likewise, the lower-level drying due to liquid water processes is determined by

$$Q(z)_{\text{low}} = \frac{\tilde{Q}_{\text{low}}(z)}{\tilde{P}_s} P_s. \tag{9}$$

Because the differences in convective heating profile shape resulting from the relative importance of liquid and ice water processes that vary from case to case become prominent for higher PTH (see Fig. 6 of Part II), the separate determination of the upper-level and lower-level heating amplitudes has been only applied to convective rain with PTHs that are 3 km higher than the separating level in Part II. The above procedure of Q_{2p} retrieval is also applied to convective rain with the same PTH as the heating retrieval to maintain consistency with the heating retrieval.

For anvil regions with a PTH higher than the melting level (Fig. 4d), on the other hand, the Q_{2p} profile corresponding to P_m is selected in the anvil Q_{2p} profile lookup table (Fig. 3c). The upper-level drying amplitude is then determined by

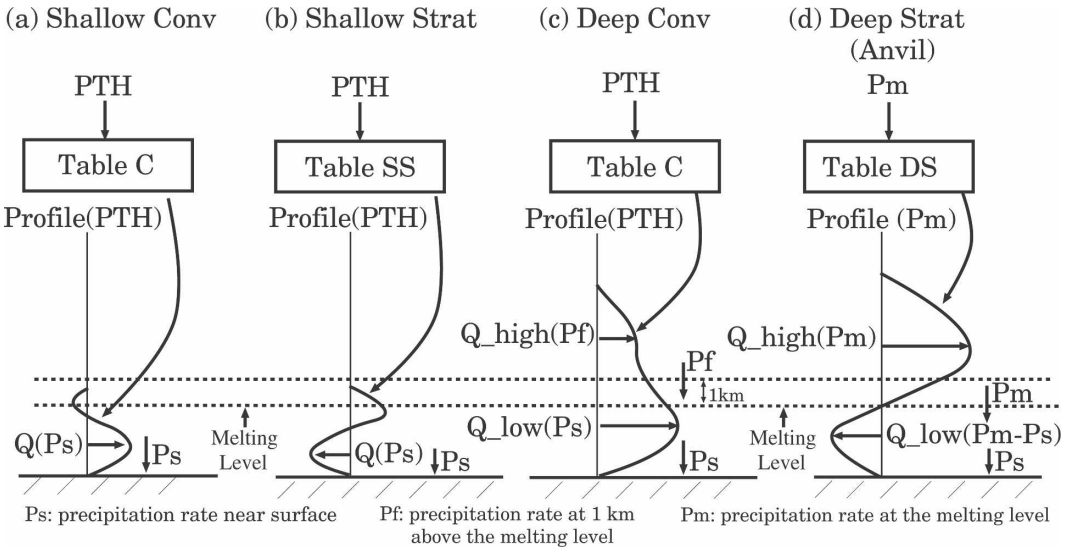

FIG. 4. Diagram showing the procedure for deriving Q_{2p} profiles using the SLH algorithm. See the text for details.

$$Q_{\text{high}}(z) = \frac{\tilde{Q}_{\text{high}}(z)}{\tilde{P}_m} P_m. \tag{10}$$

The evaporative moistening rate below the melting level in the anvil regions is proportional to the reduction of the precipitation profile toward the surface from the melting level. The downward decrease of the intensity of anvil rain below the melting layer has been statistically indicated in the PR observation (see Fig. 2 of Takayabu 2002) as well as in case studies of traditional radar observations (e.g., Leary and Houze 1979). Thus, the algorithm computes the lower-level moistening amplitude Q_{low} as a function of the difference of rainfall rate between the surface and the melting level $P_m - P_s$:

$$Q_{\text{low}}(z) = \frac{\tilde{Q}_{\text{low}}(z)}{\tilde{P}_m - \tilde{P}_s} (P_m - P_s). \tag{11}$$

The above procedure allows us to estimate the Q_{2p} profiles in the anvil regions both with and without surface precipitation. For a given P_m, the algorithm computes stronger lower-level moistening for anvil regions without surface rain than for anvil regions with surface rain. The Q_{2p} profile is shifted up or down by matching the melting level of the COARE lookup table with the observed one, as in the heating retrieval.

5. Consistency check

a. Time-averaged profiles

Four 8-day periods from TOGA COARE (19–26 December 1992), GATE (1–8 September 1974), SCSMEX NESA (2–9 June 1998), and KWAJEX (6–13 September 1999) are used for a consistency check of the SLH algorithm, as shown in Fig. 5. For each period, Q_{2p} profiles were reconstructed using the simulated parameters (i.e., convective/stratiform classification, PTH, P_s, P_m, and P_f) as input. The algorithm-reconstructed Q_{2p} profiles from the GCE-simulated precipitation profiles are compared with GCE-simulated true Q_2 profiles for the convective, stratiform, nonprecipitating, and total regions.

For the COARE case, the SLH algorithm with the COARE lookup table produces good agreement between the SLH-reconstructed Q_{2p} and GCE-simulated Q_2 profiles for convective and stratiform regions (Fig. 5a). The reconstructed total Q_{2p} profile is in good agreement with the model except for the lowest levels where moistening due to nonprecipitating processes is dominant.

For the GATE case, the COARE lookup table results in less agreement between the SLH-reconstructed and GCE-simulated profiles for convective and stratiform regions (Fig. 5b). The SLH-reconstructed drying at z = 1–3 km is weaker than the GCE-simulated drying for the convective region, whereas the SLH-reconstructed moistening at z = 1–3 km is weaker than the GCE-simulated moistening for the stratiform region. Despite compensating errors at z = 1–3 km from each component (convective and stratiform), the SLH-reconstructed drying at z = 2–6 km is stronger than the GCE-simulated drying for the total region. This discrepancy is mostly explained by moistening in nonprecipitating regions that SLH cannot reconstruct.

The COARE lookup table produces good agreement between reconstructed Q_{2p} and simulated Q_2 profiles for the SCSMEX convective and stratiform regions

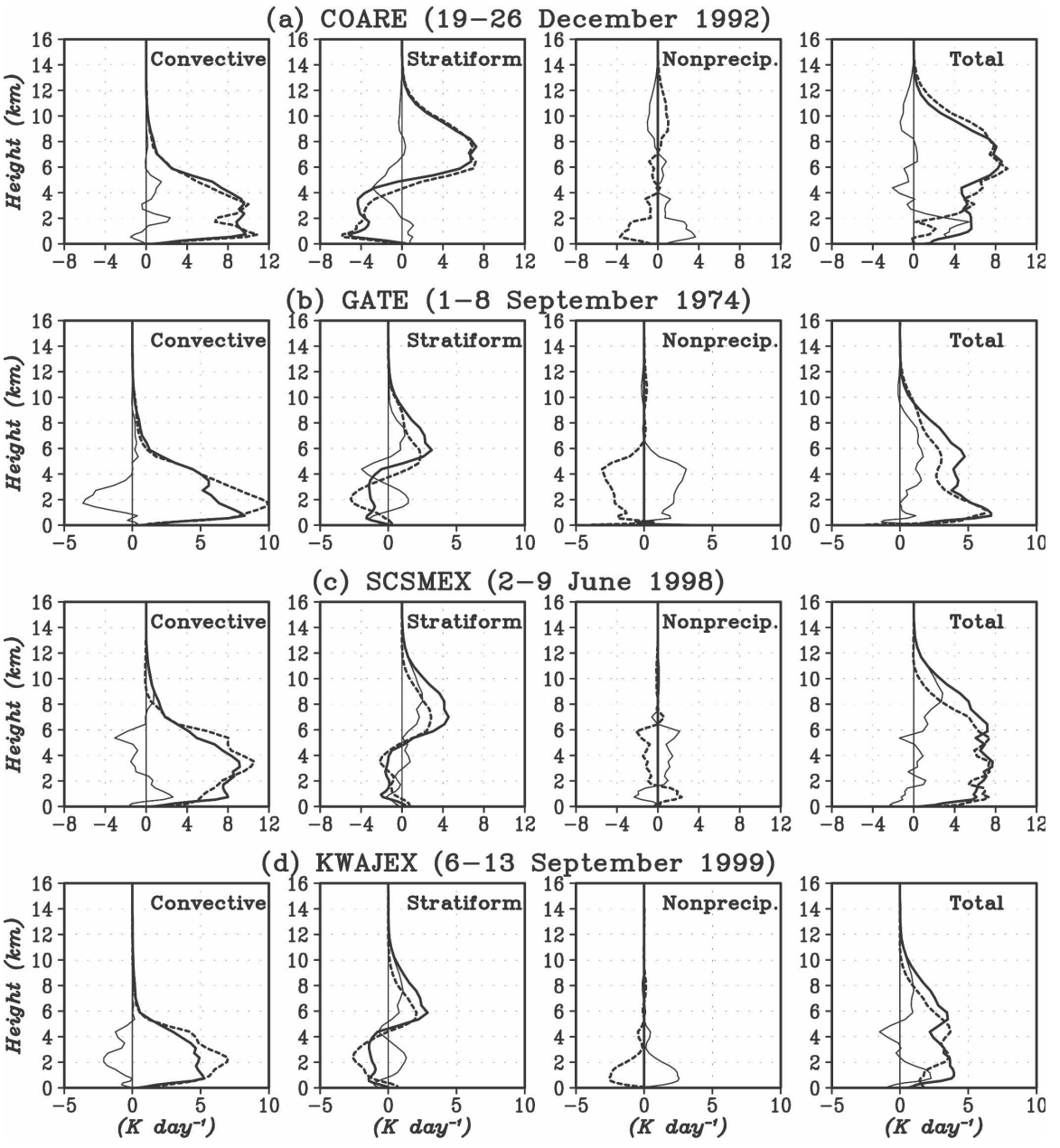

FIG. 5. Eight-day-averaged profiles of Q_{2p} reconstructed by the SLH algorithm with the COARE lookup table (thick solid line) and Q_2 simulated by the GCE model (dotted line) for the (a) COARE 19–26 Dec 1992 case, (b) GATE 1–8 Sep 1974 case, (c) SCSMEX NESA 2–9 Jun 1998 case, and (d) KWAJEX 6–13 Sep 1999 case for (left) the convective regions, (center left) the stratiform regions, (center right) the nonprecipitating regions, and (right) the total regions. Thin solid lines indicate differences between the SLH-reconstructed profile and the GCE-simulated profile.

(Fig. 5c). In addition to good agreement for the convective and stratiform regions, the contribution of the nonprecipitating region to the SCSMEX total Q_2 profile is small, leading to good agreement for the reconstructed Q_{2p} and simulated Q_2 profiles for the SCSMEX total region.

For the KWAJEX case, the SLH-reconstructed drying below $z = 4$ km is weaker than the GCE-simulated drying for the convective Q_2 profiles, whereas the SLH-reconstructed moistening below $z = 4$ km is weaker than the GCE-simulated moistening for the stratiform Q_2 profiles, similar to the GATE case. Because of compensating errors below $z = 4$ km from each component (convective and stratiform), the reconstructed total Q_{2p}

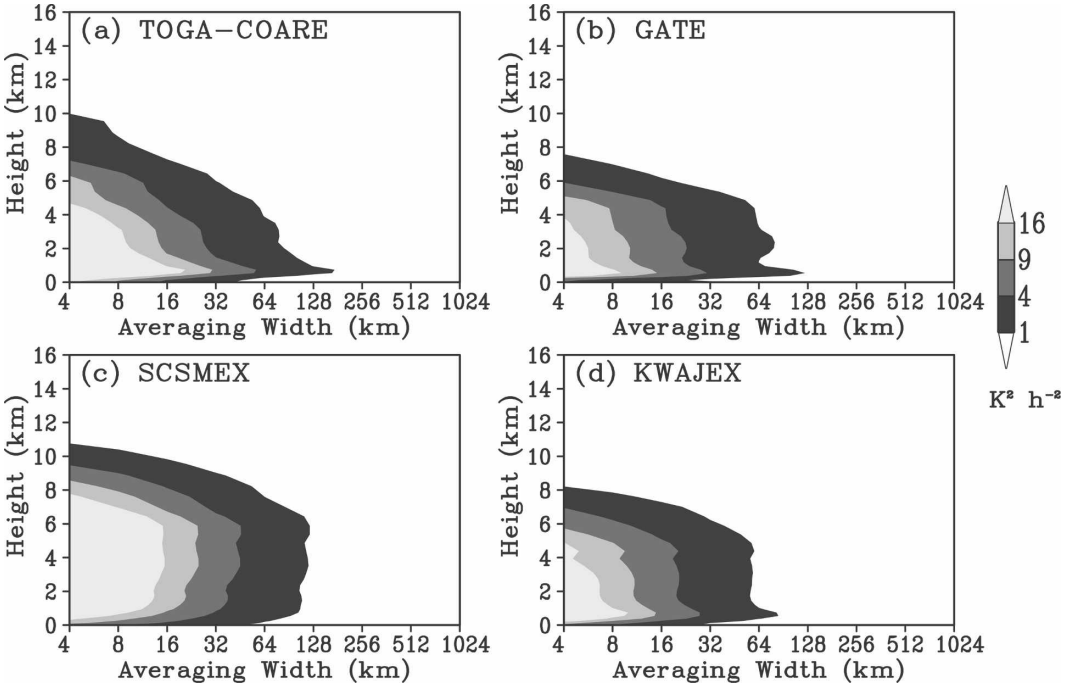

FIG. 6. The rms error in the horizontally averaged profiles between the SLH algorithm-reconstructed Q_{2p} and the GCE-simulated Q_2 for the (a) COARE, (b) GATE, (c) SCSMEX, and (d) KWAJEX cases.

profile is in good agreement with the model except for the lowest levels where moistening due to nonprecipitating processes is dominant.

The differences between the SLH-reconstructed Q_{2p} and GCE-simulated Q_2 shown here are larger than those between the SLH-reconstructed Q_{1Rp} and GCE-simulated Q_{1R} (Part II, their Fig. 9). This is because the Q_2 profiles are noisier than those of Q_{1R} because of larger contributions from eddy fluxes. The SLH algorithm cannot estimate the effect (moistening) of the nonprecipitating area, which also leads to a discrepancy with the GCE results. Nevertheless, the SLH-reconstructed total Q_{2p} profiles are in good agreement with the GCE-simulated ones, especially for the case in which the contribution of the nonprecipitating region to the Q_2 budget is small.

b. Error estimation

In the SLH algorithm, lookup tables are constructed based on the assumption that Q_{2p} profiles correspond statistically to precipitation profiles or precipitation parameters (i.e., convective/stratiform classification, PTH, P_s, P_m, and P_f). However, the instantaneous gridcell relationship between precipitation profiles and Q_{2p} is somewhat ambiguous. Part II performed a preliminary evaluation of the horizontally averaged estimates and found that horizontal averaging over an ~30-km width was required to reduce random errors in the SLH-reconstructed heating profiles to acceptable levels.

Following the method of Part II, a preliminary evaluation of the horizontally averaged estimates of Q_{2p} for the COARE, GATE, SCSMEX, and KWAJEX periods used in the consistency check is performed. The Q_{2p} profiles were reconstructed grid by grid for each 8-day period using the simulated parameters as input. The differences between the reconstructed Q_{p2} profiles and the simulated Q_2 were then examined statistically to find the errors in the instantaneous gridcell estimates using the table method. Larger root-mean-square (rms) errors were found for Q_{2p} (Fig. 6) than for Q_{1Rp} (Part II, their Fig. 10). Although the rms errors of Q_{1Rp} at the PR footprint scale (4 km) are smaller than 16 K^2 h^{-2}, those of Q_{2p} are much larger than 16 K^2 h^{-2}. A major reason is the larger contribution of eddy fluxes in the Q_{2p} budget than in the Q_{1Rp} budget. Averaging over ~60 km in width reduces the rms to about 1 K^2 h^{-2}. From these results, averaging over ~60 km in width is recommended in order to use the SLH algorithm estimates of Q_2 quantitatively.

6. PR applications

In this section, the Q_{2p} retrieval is applied to precipitation profiles from version 6 of the TRMM PR 2A25

dataset (Iguchi 2007), which is instantaneous and at footprint-scale (i.e., a level-2 product). Shige et al. (2006) recently investigated the consistency between TMI-observed brightness temperatures (TBs) and those simulated from PR2A25 version-5 (V5) and version-6 (V6) rain profiles over the central Pacific using a radiative transfer model. They showed that simulated TBs from PR V6 exhibits better agreement with observed ones than those from PR V5, implying the algorithm improvements. For stratiform regions, the Q_{2p} profile is shifted by matching the melting level of the COARE lookup table with the observed climatological melting level. Brightband height estimates from version 6 of TRMM PR 3A25, 5°-spatial-resolution gridded monthly composite of instantaneous and footprint-scale data (PR 2A25), are also used as the melting levels.

a. Comparison of Q_2 profiles over the SCSMEX NESA region

In Part II, the accuracy of the SLH-retrieved heating was evaluated by comparison with a rawinsonde-based analysis of diabatic heating for the SCSMEX NESA derived by Johnson and Ciesielski (2002). Key features of the vertical profiles agree well—in particular, the level of maximum heating. Here, the accuracy of the SLH-retrieved Q_{2p} is evaluated by comparing with a rawinsonde-based analysis of Q_2 for the SCSMEX NESA derived by Johnson and Ciesielski (2002).

Figure 7 shows a comparison between SLH-retrieved Q_{2p} from version 6 of the TRMM PR datasets and sounding-based Q_2 during the campaign's most convectively active period (15 May–20 June 1998). This period also coincides with the time during which the budget analysis was considered to be most reliable because of the completeness of the sounding network. Mapes et al. (2003) suggested that averages of about 30 days reduce sampling errors in the rainfall-rate estimate (proportional to integrated Q_1 or Q_2) to 10% for the SCSMEX NESA. There is very good agreement in several key features of the vertical profiles—in particular, below the melting level (5 km). It is evident from Fig. 7 that the Q_{2p} drying magnitudes are smaller than the sounding-derived magnitudes in the upper troposphere above 9 km. The Q_{2p} estimates from PR data are subject to sampling errors caused by the PR's narrow swath width (~215 km), leading to a discrepancy with the sounding estimates (see Grecu and Olson 2006, their Fig. 9). The SLH algorithm is severely limited by the inherent sensitivity of the PR, which can detect only precipitation-sized particles. During the growing phase of a congestus cloud, the cloud top and radar-echo top may correlate well (Kingsmill and Wakimoto 1991). However, during the decaying phase of a cumulonimbus cloud, the two tops may differ considerably, leading to an underestimation of drying in the upper troposphere. The lookup table for the anvil based on P_m (Fig. 3c) does not fully capture the variability in the upper-level drying of the stratiform rain region, which also accounts for the underestimation of drying in the upper troposphere.

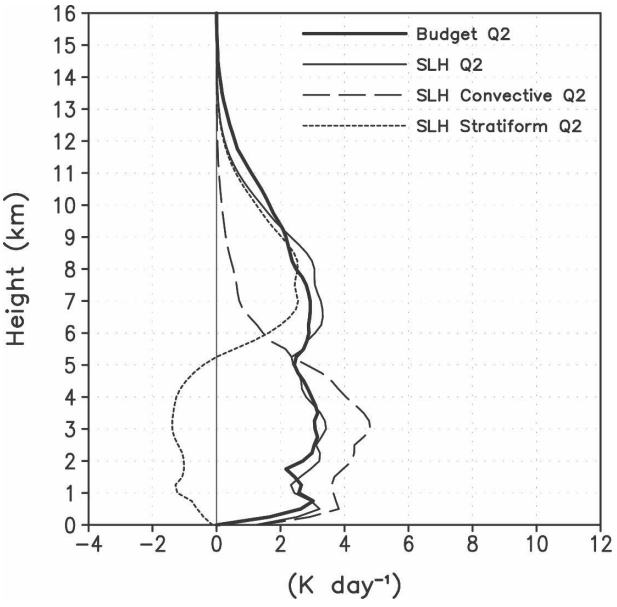

FIG. 7. The Q_2 profiles from diagnostic calculations (Johnson and Ciesielski 2002) and the SLH algorithm using version 6 of the TRMM PR datasets for SCSMEX (15 May–20 Jun 1998).

b. El Niño–La Niña

Figures 8a,b show the monthly mean surface rainfall (mm day^{-1}) for February 1998 and February 1999, respectively. Drying/moistening structures over the six oceanic regions (western Pacific, central Pacific, eastern Pacific, South Pacific, Indian Ocean, and Atlantic Ocean) shown in Fig. 8 will be examined and compared. Heating structures over the same regions were examined in Part II.

Figures 9 and 10 show the monthly mean convective, stratiform, and total Q_{2p} profiles derived from the SLH algorithm for six locations over the tropical oceans for February 1998 and February 1999, respectively. Total Q_{1Rp} profiles derived from the SLH algorithm are also shown. Note that the total Q_{1Rp} profiles are not the same as in Part II but are estimated using the Q_{1Rp} profile lookup tables derived from the TOGA COARE simulations made with the TOGA COARE flux algorithm (Fairall et al. 1996; Wang et al. 1996) and a modification of conversion of cloud ice to snow in the ice

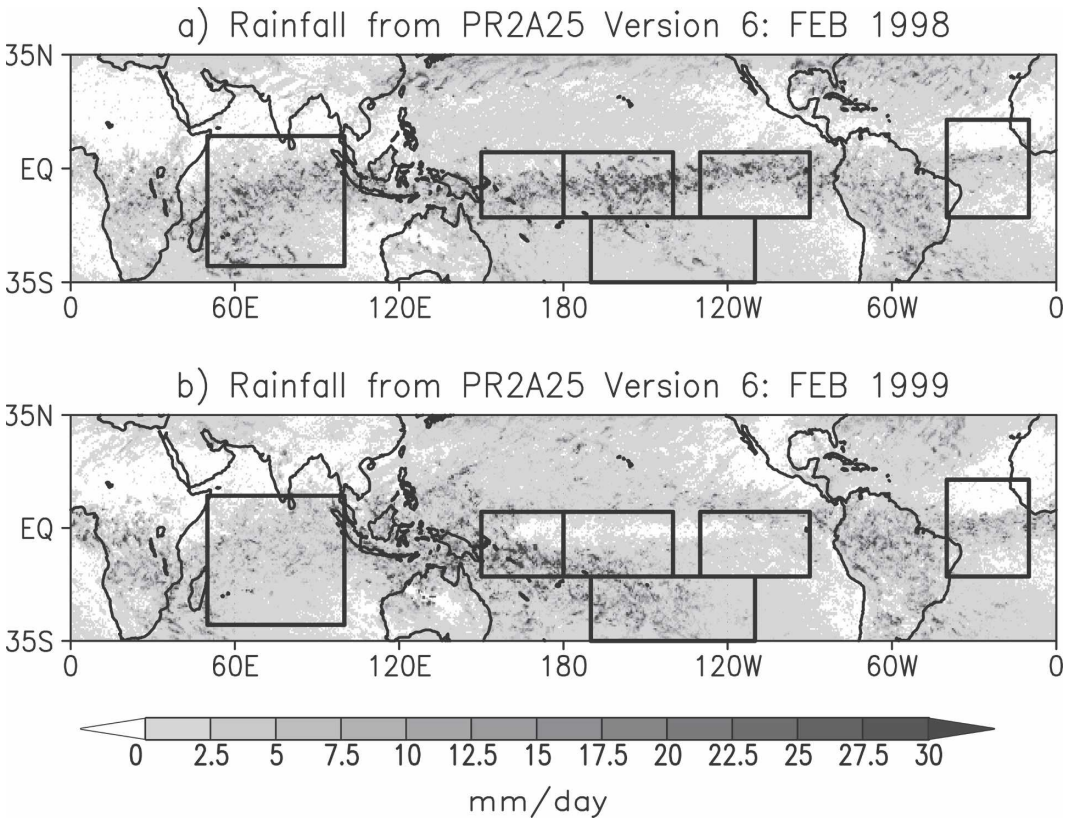

FIG. 8. Monthly mean rainfall (mm day^{-1}) derived from PR2A25, version 6, for (a) February 1998 and (b) February 1999. The drying/moistening profiles will be compared and examined for the various geographic locations identified by the boxes. (Figure is from Part II.)

microphysics schemes (Tao et al. 2003). However, the differences are very small.

A maximum at low levels (~0.5 km) is found in the SLH-estimated total Q_{2p} profile over the western Pacific for February 1998 (Fig. 9a). This low-level maximum in the SLH-estimated total Q_{2p} profile comes from the SLH-estimated convective Q_{2p} profile with a low-level maximum, reflecting the abundance of shallow convection. Diagnostic budget studies over western Pacific regions (Reed and Recker 1971; Nitta 1972; Yanai et al. 1973; Lin and Johnson 1996) indicate a double-peak structure with a minimum near 4 km. Whereas the SLH-estimated mean Q_{2p} profile for February 1999 shows a minimum near 4.5 km, the SLH-estimated mean Q_{2p} profile with the low-level maximum for February 1998 does not resemble those determined from the diagnostic budget studies. Note that diagnostic budget studies over the western Pacific do not contain periods corresponding to the warm phases of ENSO, except for 2 months in the period from March to July of 1958 in Nitta (1972). The SLH-estimated mean Q_{2p} profile for February 1998 resembles the mean Q_2 profile with a lower-level maximum over the GATE region (Nitta 1978; Thompson et al. 1979), which is due to a different cloud population with more shallow convection and lower sea surface temperatures (SSTs) in the GATE region. Deep convection over the western Pacific is suppressed during the warm phase of ENSO (February 1998) relative to the cold phase (February 1999) because of lower SSTs. Thus, the difference in the SLH-estimated mean Q_{2p} profile between February 1998 and February 1999 may be reasonable.

There are dramatic differences in total Q_{2p} profiles over the central and eastern Pacific between the 1998 El Niño event and the 1999 La Niña event. First, these differences can be attributed to those in stratiform rain fraction (Schumacher and Houze 2003a). Second, the shape of convective Q_{2p} profiles also affects total Q_{2p} profiles. The convective Q_{2p} profiles are shallower during La Niña than El Niño.

Part II pointed out that the SLH-estimated heating profile over the South Pacific for February 1998 is very similar to the vertical distribution of heating during the undisturbed BOMEX period in the trade wind belts (Nitta and Esbensen 1974) and to that during episodic trade wind regimes over the western Pacific (Johnson

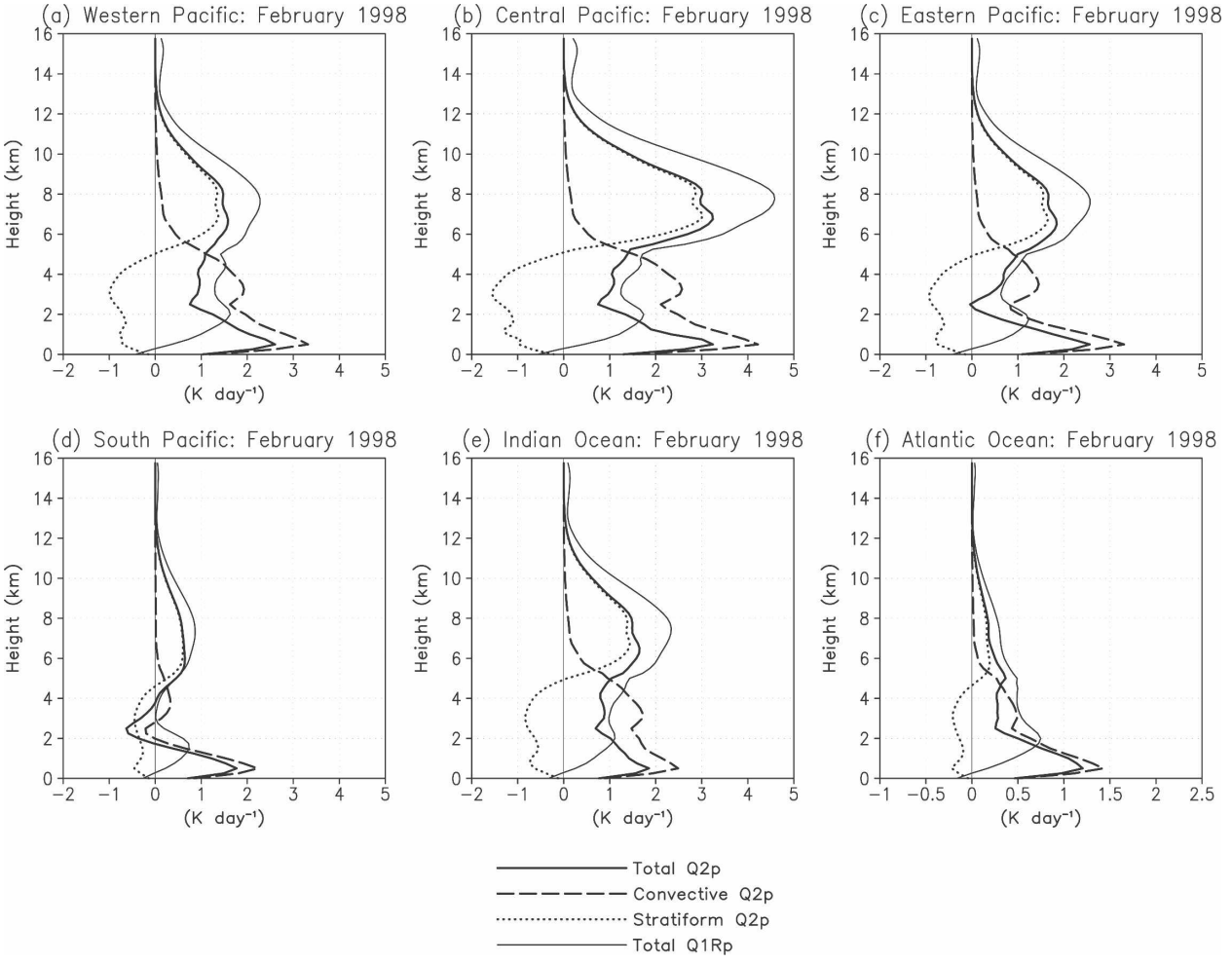

FIG. 9. Monthly (February 1998) mean total, convective, and stratiform Q_{2p} profiles derived from the SLH algorithm for various locations. Total Q_{1Rp} profiles derived from the SLH algorithm are also shown. The geographic areas are the (a) western Pacific, (b) central Pacific, (c) eastern Pacific, (d) South Pacific, (e) Indian, and (f) Atlantic Oceans. Note that the abscissa scales are the same except in (f).

and Lin 1997). On the other hand, the SLH-estimated Q_{2p} profile with low-level drying over the South Pacific for February 1998 is not similar to the vertical distribution of Q_2 with low-level moistening during the undisturbed BOMEX and to that during episodic trade wind regimes over the western Pacific. A possible reason for the differences is that the contribution from the nonprecipitating region to the Q_2 budget, which SLH cannot retrieve, is large. Another reason is that there is larger geographical variability in Q_2 profiles than in Q_1 profiles. For example, Lin and Johnson (1996) indicated that, although the heating profiles over different regions of the western Pacific warm pool are similar to one another, the drying/moistening profiles are significantly different.

The SLH-estimated Q_{2p} profiles over the Atlantic Ocean for February 1998 and February 1999 resemble the mean Q_2 profile with a lower-level maximum that was determined from a diagnostic budget study during GATE (Nitta 1978; Thompson et al. 1979) and simulated by the GCE model (see Fig. 5b). It is somewhat awkward to compare February Q_2 profiles in the Atlantic Ocean with published Q_2 profiles from GATE, which occurred in boreal summer. Also, the selected area for the Atlantic Ocean includes the trade wind area (Augstein et al. 1973) where the Q_1 and Q_2 profiles should be different from those from GATE. For a more direct comparison with the GATE profiles, the SLH-estimated Q_{1Rp} and Q_{2p} profiles over the area from 5° to 15°N latitude and from 20° to 30°W longitude, which roughly corresponds to the GATE region, are shown in Fig. 11. There is a good agreement in the key features of the Q_{2p} profiles—in particular, for the levels of maximum drying. Thus, it is shown that the

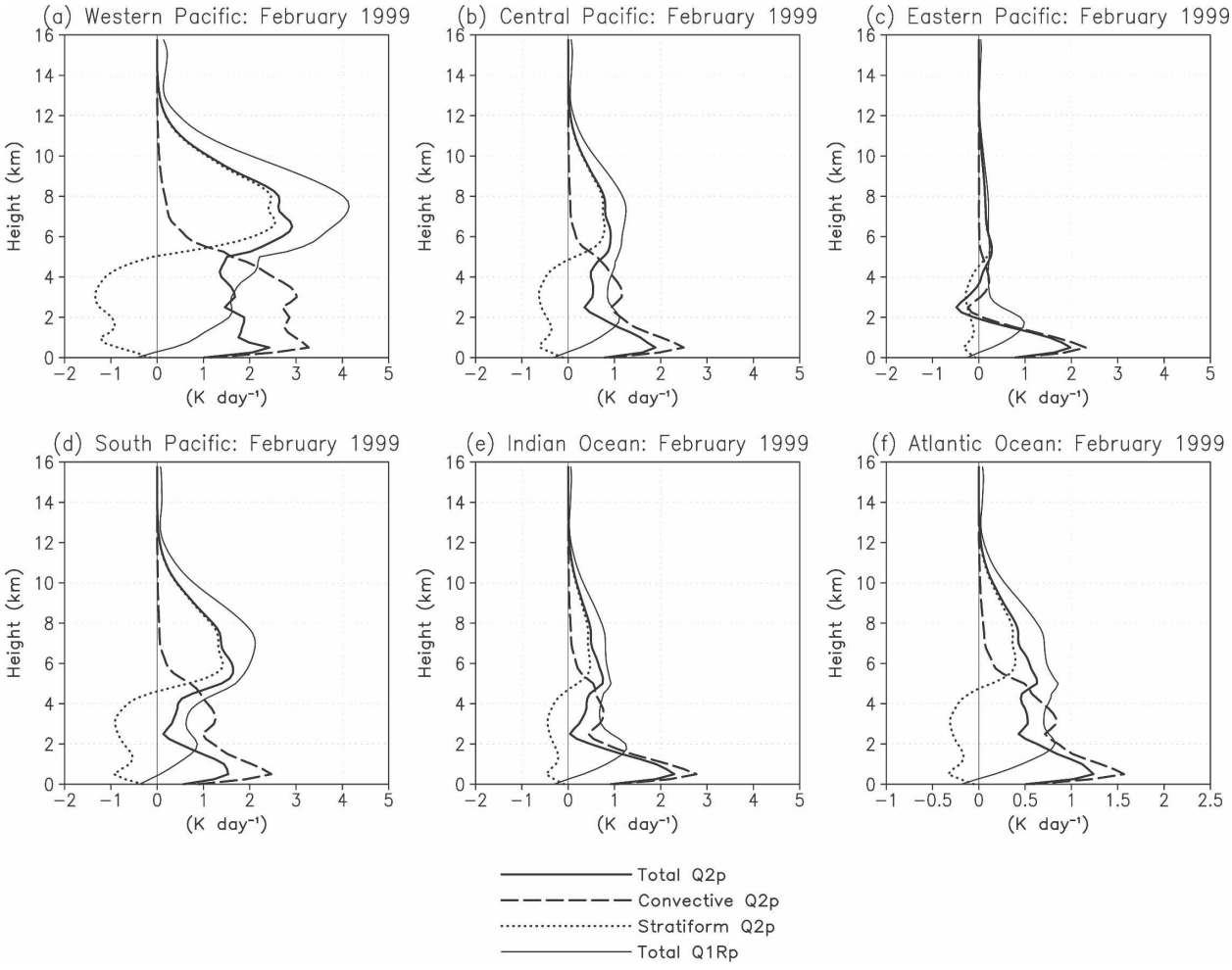

FIG. 10. As in Fig. 9, but for February 1999.

SLH algorithm can estimate differences in Q_{2p} between the western Pacific and the Atlantic Ocean as well as those in Q_1, which are also consistent with the results from the budget study (Thompson et al. 1979; see a review by Cotton and Anthes 1989).

Over the Indian Ocean, even indirect validation using the results of diagnostic studies for different years is difficult because of the lack of observations.[1] The SLH-estimated Q_{2p} profile shape over the Indian Ocean for February 1998 resembles that over the western Pacific for February 1999, whereas that over the Indian Ocean for February 1999 resembles that over the Atlantic Ocean. The differences in the SLH-estimated Q_{2p} over the Indian Ocean between February 1998 and February 1999 are consistent with those in the SLH-estimated Q_{1R} over the Indian Ocean between February 1998 and February 1999.

c. *Variability of Q_{2p} profile*

The average profiles shown in Figs. 9 and 10 may not be very representative because there are large spatial and temporal variabilities in rainfall over a larger region such as those selected in Fig. 8. Following the approach used in Part II, we used contoured frequency by altitude diagrams (CFADs; Yuter and Houze 1995) to provide the actual variability of drying/moistening profile shapes.

Many of the negative values in the low-to-middle troposphere in Figs. 12a–e and Figs. 13a,b,d are associated with evaporation in the stratiform region, suggesting large variability in stratiform rain fraction over the regions. The distinct peak in the frequency of drying at levels below 2 km is also evident for all six geographic

[1] Nitta (1980, 145–150) did preliminary budget computations over the Bay of Bengal for a very short time (a 3-day period).

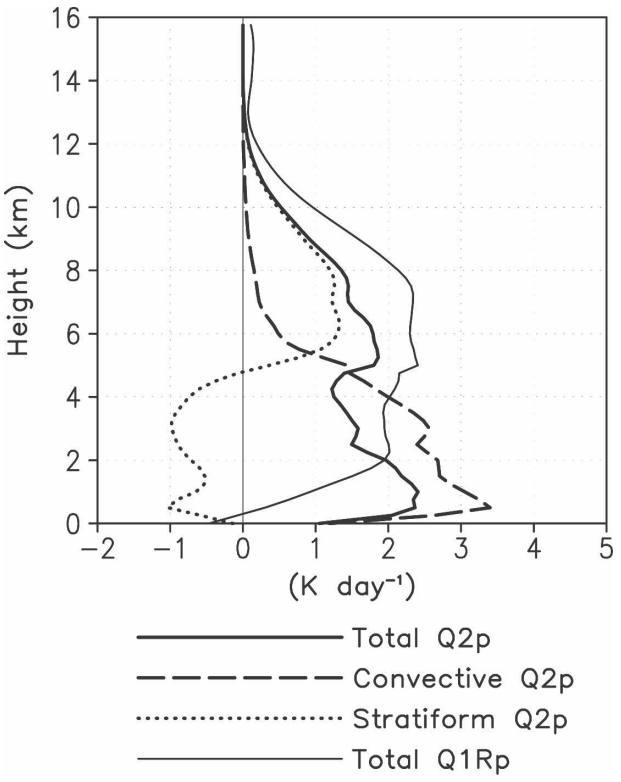

FIG. 11. As in Fig. 9, but for September 1999 over the GATE region from 5° to 15°N latitude and from 20° to 30°W longitude.

areas for both February 1998 and February 1999 in the CFADs (Figs. 12 and 13), corresponding to a drying peak at the lowest levels seen in the mean convective Q_{2p} profiles (Figs. 9 and 10). It is inferred from the convective Q_{2p}-profile lookup table (Fig. 3a) that shallow convection with PTHs lower than 4 km accounts for this distinct peak.

The CFADs of mean Q_1 and Q_2 over the intensive flux array during TOGA COARE based on a 6-hourly analysis have been shown by Johnson and Ciesielski (2000, their Fig. 3). Direct comparison of the CFADs shown in Figs. 12 and 13 with those in Johnson and Ciesielski (2000) cannot be done, because the CFADs shown in Figs. 12 and 13 are derived from monthly mean Q_{2p} profiles at 0.5° resolution. Still, there is a striking difference. In the CFAD of Q_2 in Johnson and Ciesielski (2000), there is some contribution to negative values of Q_2 in the lowest 2 km from shallow cumulus clouds and sub-cloud-layer eddies during nonprecipitating periods of the TOGA COARE intensive observing period (Johnson and Lin 1997). On the other hand, there is almost no contribution to negative values of Q_{2p} in the lowest 2 km from shallow cumulus clouds and sub-cloud-layer eddies, although there is some contribution to negative values of Q_{2p} in the lowest 2 km from stratiform rain. Again, the SLH algorithm cannot retrieve moistening for a nonprecipitating region because of the sensitivity of the PR.

7. Summary and future work

In this study, the SLH algorithm was used to estimate Q_2 profiles from PR data together with Q_{1R} profiles. There are two differences between Q_{1R} and Q_2. First, the eddy moisture flux convergence is one of the major contributors to the Q_2 while the contribution to the Q_{1R} budget by the eddy heat flux convergence is minor. Second, Q_2 in the nonprecipitating region is of the same order as that in the stratiform region whereas the Q_{1R} profile in the nonprecipitating region is negligible, which is consistent with the results from Nitta and Esbensen (1974) that show that moistening rates are about a factor of 3 larger than heating/cooling rates during undisturbed periods in the trades. This is attributable to a larger contribution of eddy fluxes in Q_2 than in Q_{1R}. These two factors lead to larger errors in Q_2 than in Q_{1R}.

The Q_{2p} profiles were reconstructed from CRM-simulated parameters (i.e., convective/stratiform classification, PTH, P_s, P_m, and P_f) with the COARE table and then were compared with CRM-simulated true Q_2 profiles, which were computed directly from the water vapor equation in the model. COARE, GATE, SCSMEX, and KWAJEX periods were used for the consistency check. The consistency check indicates that discrepancies between the SLH-reconstructed Q_{2p} and GCE-simulated Q_2 profiles, especially at low levels, are larger than those between the SLH-reconstructed Q_{1Rp} and GCE-simulated Q_{1R} profiles. Larger discrepancies in Q_{2p} at low levels are due to moistening in the nonprecipitating region that SLH cannot reconstruct.

The SLH algorithm was applied to PR data, and the results were compared with Q_2 profiles derived diagnostically from SCSMEX sounding data. Although discrepancies between the SLH-retrieved and sounding-based profiles for Q_2 are larger than those for Q_{1R}, key features of the vertical profiles agree well. The Q_{2p} drying magnitudes are smaller than the sounding-derived magnitudes in the upper troposphere, which are attributable to three reasons. First, the Q_{2p} estimates from PR data are subject to sampling errors that result from the PR's narrow swath width (~215 km). Second, the SLH algorithm is severely limited by the inherent sensitivity of the PR, which can detect only precipitation-sized particles. Third, the lookup table for the anvil based on P_m does not fully capture the variability in the upper-level drying of the stratiform rain region.

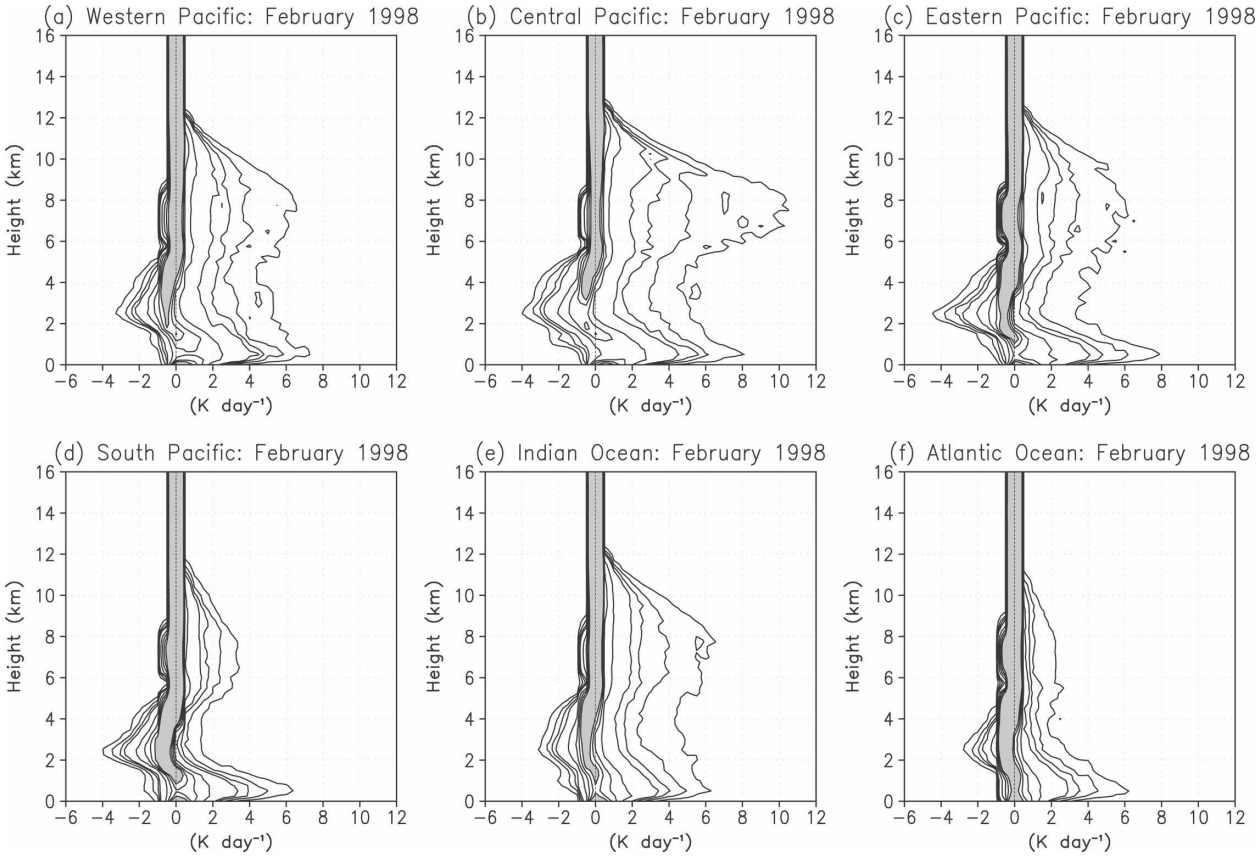

FIG. 12. CFADs of monthly (February 1998) total Q_{2p} profiles at 0.5° resolution derived from the SLH algorithm for various locations. The geographic areas are the (a) western Pacific, (b) central Pacific, (c) eastern Pacific, (d) South Pacific, (e) Indian, and (f) Atlantic Oceans. The bin size is 0.5 K. CFAD contour interval is 1% for values of less than 4% and is 4% for values greater than 4%, with values of greater than 20% being shaded.

The SLH algorithm was also applied to PR data for February 1998 (El Niño) and February 1999 (La Niña). The differences in the SLH-estimated Q_{2p} between February 1998 and February 1999 are consistent with those in the SLH-estimated Q_{1R} between February 1998 and February 1999. It is shown that the SLH algorithm can estimate differences of Q_{2p} between the western Pacific Ocean and the Atlantic Ocean as well as those of Q_{1p} that are consistent with budget results (Thompson et al. 1979; see a review by Cotton and Anthes 1989).

Although the SLH-estimated heating profile over the South Pacific for February 1998 is very similar to the vertical distribution of heating during the undisturbed BOMEX period in the trade wind belts (Nitta and Esbensen 1974) and that during episodic trade wind regimes over the western Pacific (Johnson and Lin 1997), the SLH-estimated Q_{2p} profile with low-level drying over the South Pacific for February 1998 is not similar to the vertical distribution of Q_2 with low-level moistening during the undisturbed BOMEX and that during episodic trade wind regimes over the western Pacific. A possible reason is that SLH cannot retrieve moistening for a nonprecipitating region because of the sensitivity of the PR. Measurements from other sensors will have to be integrated to obtain a more accurate estimation of Q_2 profiles. For example, TRMM Visible and Infrared Scanner data provide information on the population of shallow, nonprecipitating cumulus clouds that have important moistening effects, thereby, perhaps, helping in the retrieval of Q_2 profiles.

In this study, the two-dimensional version of the GCE model was used. Real clouds and cloud systems are three-dimensional. The availability of exponentially increasing computer capabilities has resulted in three-dimensional CRM simulations for multiday periods with large horizontal domains becoming increasing prevalent. Larger temporal variability in the two-dimensional simulation than in the three-dimensional simulation was found by Grabowski et al. (1998), Donner et al. (1999), and Zeng et al. (2007). Tao et al. (2000) pointed out that the GCE three-dimensional

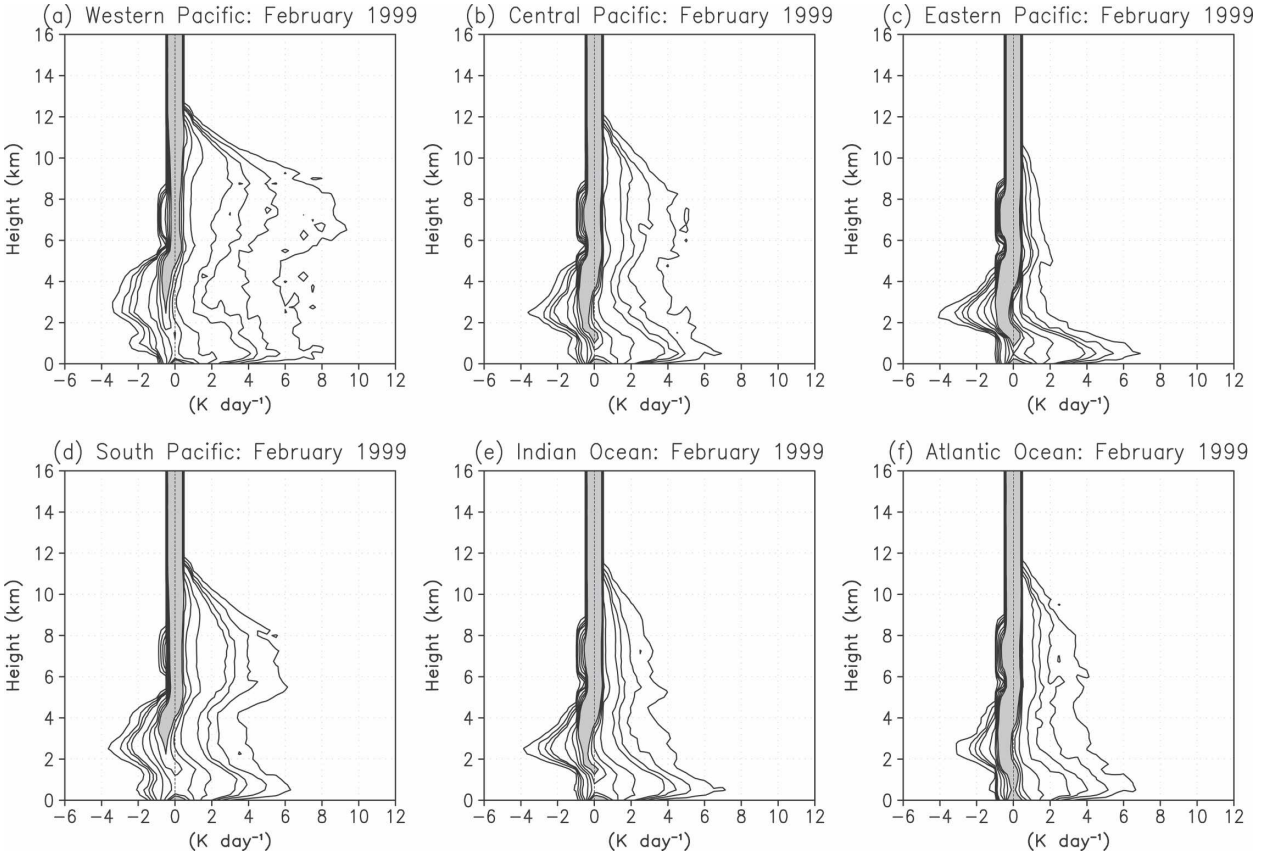

FIG. 13. As in Fig. 12, but for February 1999.

model-simulated Q_2 budget is in better agreement with observations in the lower troposphere than is its two-dimensional counterpart. We are now performing the three-dimensional CRM simulations to compare lookup tables from the two- and three-dimensional CRM simulations.

Acknowledgments. This study is supported by the Japan Aerospace Exploration Agency/Earth Observation Research Center (JAXA/EORC) TRMM project. The first author is also supported by funding from JST Corporation–Core Research for Evolution Science and Technology (CREST). He thanks Prof. Richard Johnson of the Colorado State University for his comments. Yukari N. Takayabu expresses her heartfelt gratitude to the late Prof. Tsuyoshi Nitta for motivating her to develop the latent heating algorithm utilizing TRMM PR data. Author W.-K. Tao is mainly supported by the NASA Headquarters (HQ) Atmospheric Dynamics and Thermodynamics Program and the NASA TRMM. He thanks Dr. R. Kakar at NASA HQ for his support of GCE development over the past decade. The authors thank two anonymous reviewers for their constructive comments, which improved the clarity of the presentation in this paper. The TRMM products in this paper were provided by JAXA. The Grid Analysis and Display System (GrADS) package was utilized for the figures.

REFERENCES

Ackerman, T. P., and G. M. Stokes, 2003: The Atmospheric Radiation Measurement Program. *Phys. Today,* **56,** 38–44.

Augstein, E., H. Riehl, F. Ostapoff, and V. Wagner, 1973: Mass and energy transports in an undisturbed Atlantic trade-wind flow. *Mon. Wea. Rev.,* **101,** 101–111.

Awaka, J., H. Kumagai, T. Iguchi, and K. Okamoto, 1996: Development of an algorithm for classifying rain types (in Japanese). *J. Commun. Res. Lab.,* **42,** 325–337.

——, T. Iguchi, and K. Okamoto, 1998: Early results on rain type classification by the Tropical Rainfall Measuring Mission (TRMM) precipitation radar. *Proc. Eighth URSI Commission F Open Symp.,* Aveiro, Portugal, URSI, 143–146.

——, ——, and ——, 2007: Rain type classification algorithm. *Measuring Precipitation from Space—EURAINSAT and the Future,* V. Levizzani, P. Bauer, and F. J. Turk, Eds., Springer, 213–224.

Back, L. E., and C. S. Bretherton, 2006: Geographic variability in the export of moist static energy and vertical motion profiles in the tropical Pacific. *Geophys. Res. Lett.,* **33,** L17810, doi:10.1029/2006GL026672.

Braun, S. A., and R. A. Houze Jr., 1995: Melting and freezing in a mesoscale convective system. *Quart. J. Roy. Meteor. Soc.,* **121,** 55–77.

Caniaux, G., J.-L. Redelsperger, and J.-P. Lafore, 1994: A numerical study of the stratiform region of a fast-moving squall line. Part I: General description and water and heat budgets. *J. Atmos. Sci.,* **51,** 2046–2074.

Chong, M., and D. Hauser, 1989: A tropical squall line observed during the COPT81 experiment in West Africa. Part II: Water budget. *Mon. Wea. Rev.,* **117,** 728–744.

——, and ——, 1990: A tropical squall line observed during the COPT81 experiment in West Africa. Part III: Heat and moisture budgets. *Mon. Wea. Rev.,* **118,** 1696–1706.

Cotton, W. R., and R. A. Anthes, 1989: *Storm and Cloud Dynamics.* Academic Press, 883 pp.

Donner, L. J., C. J. Seman, and R. S. Hemler, 1999: Three-dimensional cloud-system modeling of GATE convection. *J. Atmos. Sci.,* **56,** 1885–1912.

Fairall, C., E. F. Bradley, D. P. Rogers, J. B. Edson, and G. S. Young, 1996: Bulk parameterization of air-sea fluxes for TOGA COARE. *J. Geophys. Res.,* **101,** 3747–3764.

Gallus, W. A., Jr., and R. H. Johnson, 1991: Heat and moisture budgets of an intense midlatitude squall line. *J. Atmos. Sci.,* **48,** 122–146.

Gamache, J. F., and R. A. Houze Jr., 1983: Water budget of a mesoscale convective system in the Tropics. *J. Atmos. Sci.,* **40,** 1835–1850.

Grabowski, W. W., X. Wu, M. W. Moncrieff, and W. D. Hall, 1998: Cloud-resolving modeling of tropical cloud systems during Phase III of GATE. Part II: Effects of resolution and the third spatial dimension. *J. Atmos. Sci.,* **55,** 3264–3282.

Grecu, M., and W. S. Olson, 2006: Bayesian estimation of precipitation from satellite passive microwave observations using combined radar–radiometer retrievals. *J. Appl. Meteor. Climatol.,* **45,** 416–433.

Guichard, F., J.-P. Lafore, and J.-L. Redelsperger, 1997: Thermodynamical impact and internal structure of a tropical convective cloud system. *Quart. J. Roy. Meteor. Soc.,* **123,** 2297–2324.

Heymsfield, G. M., B. Geerts, and L. Tian, 2000: TRMM precipitation radar reflectivity profiles as compared with high-resolution airborne and ground-based radar measurements. *J. Appl. Meteor.,* **39,** 2080–2102.

Houze, R. A., Jr., and A. K. Betts, 1981: Convection in GATE. *Rev. Geophys. Space Phys.,* **19,** 541–576.

——, C.-P. Cheng, C. A. Leary, and J. F. Gamache, 1980: Diagnosis of cloud mass and heat fluxes from radar and synoptic data. *J. Atmos. Sci.,* **37,** 754–773.

Iguchi, T., 2007: Space-borne radar algorithms. *Measuring Precipitation from Space—EURAINSAT and the Future,* V. Levizzani, P. Bauer, and F. J. Turk, Eds., Springer, 199–212.

——, and R. Meneghini, 1994: Intercomparison of single-frequency methods for retrieving a vertical rain profile from airborne or spaceborne radar data. *J. Atmos. Oceanic Technol.,* **11,** 1507–1516.

——, T. Kozu, R. Meneghini, J. Awaka, and K. Okamoto, 2000: Rain-profiling algorithm for the TRMM precipitation radar. *J. Appl. Meteor.,* **39,** 2038–2052.

Johnson, R. H., 1976: The role of convective-scale precipitation downdrafts in cumulus and synoptic-scale interactions. *J. Atmos. Sci.,* **33,** 1890–1910.

——, 1984: Partitioning tropical heat and moisture budgets into cumulus and mesoscale components: Implications for cumulus parameterization. *Mon. Wea. Rev.,* **112,** 1590–1601.

——, and G. S. Young, 1983: Heat and moisture budgets of tropical mesoscale anvil clouds. *J. Atmos. Sci.,* **40,** 2138–2146.

——, and X. Lin, 1997: Episodic trade wind regimes over the western Pacific warm pool. *J. Atmos. Sci.,* **54,** 2020–2034.

——, and P. E. Ciesielski, 2000: Rainfall and radiative heating rates from TOGA COARE atmospheric budgets. *J. Atmos. Sci.,* **57,** 1497–1514.

——, and ——, 2002: Characteristics of the 1998 summer monsoon onset over the northern South China Sea. *J. Meteor. Soc. Japan,* **80,** 561–578.

Kingsmill, D. E., and R. M. Wakimoto, 1991: Kinematic, dynamic, and thermodynamic analyses of a weakly sheared severe thunderstorm over northern Alabama. *Mon. Wea. Rev.,* **119,** 262–297.

Kozu, T., and Coauthors, 2001: Development of precipitation radar onboard the Tropical Rainfall Measuring Mission (TRMM) satellite. *IEEE Trans. Geosci. Remote Sens.,* **39,** 102–116.

Krishnamurti, T. N., S. Low-Nam, and R. Pasch, 1983: Cumulus parameterization and rainfall rates II. *Mon. Wea. Rev.,* **111,** 815–828.

Kummerow, C., and Coauthors, 2000: The status of the Tropical Rainfall Measuring Mission (TRMM) after two years in orbit. *J. Appl. Meteor.,* **39,** 1965–1982.

Lafore, J. P., J. L. Redelsperger, and G. Jaubert, 1988: Comparison between a three-dimensional simulation and Doppler radar data of a tropical squall line: Transports of mass, momentum, heat, and moisture. *J. Atmos. Sci.,* **45,** 2744–2763.

——, A. Diongue, J. L. Redelsperger, and B. Thomas, 2002: Impact of an African squall line on large scale fields of heat, moisture and momentum. Preprints, *25th Conf. on Hurricanes and Tropical Meteorology,* San Diego, CA, Amer. Meteor. Soc., 448–449.

Lang, S., W.-K. Tao, J. Simpson, and B. Ferrier, 2003: Modeling of convective–stratiform precipitation processes: Sensitivity to partitioning methods. *J. Appl. Meteor.,* **42,** 505–527.

Lau, K., and Coauthors, 2000: A report of the field operations and early results of the South China Sea Monsoon Experiment (SCSMEX). *Bull. Amer. Meteor. Soc.,* **81,** 1261–1270.

Leary, C. A., and R. A. Houze Jr., 1979: Melting and evaporation of hydrometeors in precipitation from the anvil clouds of deep tropical convection. *J. Atmos. Sci.,* **36,** 669–679.

Lin, X., and R. H. Johnson, 1996: Heating, moistening and rainfall over the western Pacific warm pool during TOGA COARE. *J. Atmos. Sci.,* **53,** 3367–3383.

Lin, Y.-L., R. D. Farley, and H. D. Orville, 1983: Bulk parameterization of the snow field in a cloud model. *J. Climate Appl. Meteor.,* **22,** 1065–1092.

Luo, H., and M. Yanai, 1984: The large-scale circulation and heat sources over the Tibetan Plateau and surrounding areas during the early summer of 1979. Part II: Heat and moisture budgets. *Mon. Wea. Rev.,* **112,** 966–989.

Mapes, B. E., 2001: Water's two height scales: The moist adiabat and the radiative troposphere. *Quart. J. Roy. Meteor. Soc.,* **127,** 2253–2266.

——, P. E. Ciesielski, and R. H. Johnson, 2003: Sampling errors in rawinsonde array budgets. *J. Atmos. Sci.,* **60,** 2697–2714.

Nesbitt, S. W., E. J. Zipser, and D. J. Cecil, 2000: A census of

precipitation features in the Tropics using TRMM: Radar, ice scattering, and lightning observations. *J. Climate,* **13,** 4087–4106.

Ninomiya, K., 1968: Heat and water budget over the Japan Sea and the Japan Islands in winter season. *J. Meteor. Soc. Japan,* **46,** 343–372.

——, 1971: Dynamical analysis of outflow from tornado-producing thunderstorms as revealed by ATS III pictures. *J. Appl. Meteor.,* **10,** 275–294.

Nitta, T., 1972: Energy budget of wave disturbances over the Marshall Islands during the years of 1956 and 1958. *J. Meteor. Soc. Japan,* **50,** 71–84.

——, 1975: Observational determination of cloud mass flux distributions. *J. Atmos. Sci.,* **32,** 73–91.

——, 1977: Response of cumulus updraft and downdraft to GATE A/B-scale motion systems. *J. Atmos. Sci.,* **34,** 1163–1186.

——, 1978: A diagnostic study of interaction of cumulus updrafts and downdrafts with large-scale motions in GATE. *J. Meteor. Soc. Japan,* **56,** 232–242.

——, 1980: Preliminary budget computations over the bay of Bengal during summer MONEX. FGGE Operations Rep. 9, Part A, World Meteorological Organization, 237 pp.

——, and S. Esbensen, 1974: Heat and moisture budget analyses using BOMEX data. *Mon. Wea. Rev.,* **102,** 17–28.

Okamoto, K., 2003: A short history of the TRMM precipitation radar. *Cloud Systems, Hurricanes and the Tropical Rainfall Measurement Mission (TRMM): A Tribute to Dr. Joanne Simpson, Meteor. Monogr.,* No. 51, Amer. Meteor. Soc., 187–195.

Petersen, W. A., and S. A. Rutledge, 2001: Regional variability in tropical convection: Observations from TRMM. *J. Climate,* **14,** 3566–3586.

Rajendran, J., T. N. Krishnamurti, V. Misra, and W.-K. Tao, 2004: An empirical cumulus parameterization scheme for a global spectral model. *J. Meteor. Soc. Japan,* **82,** 989–1006.

Reed, R. J., and E. E. Recker, 1971: Structure and properties of synoptic-scale wave disturbances in the equatorial western Pacific. *J. Atmos. Sci.,* **28,** 1117–1133.

Rutledge, S. A., and P. V. Hobbs, 1984: The mesoscale and microscale structure and organization of clouds and precipitation in midlatitude cyclones. XII: A diagnostic modeling study of precipitation development in narrow cold-frontal rainbands. *J. Atmos. Sci.,* **41,** 2949–2972.

Schumacher, C., and R. A. Houze Jr., 2003a: Stratiform rain in the Tropics as seen by the TRMM precipitation radar. *J. Climate,* **16,** 1739–1756.

——, and ——, 2003b: The TRMM precipitation radar's view of shallow, isolated rain. *J. Appl. Meteor.,* **42,** 1519–1524.

Shie, C.-L., W.-K. Tao, J. Simpson, and C.-H. Sui, 2003: Quasi-equilibrium states in the Tropics simulated by a cloud-resolving model. Part I: Specific features and budget analysis. *J. Climate,* **16,** 817–833.

Shige, S., and T. Satomura, 2000: The gravity wave response in the troposphere around deep convection. *J. Meteor. Soc. Japan,* **78,** 789–801.

——, Y. N. Takayabu, W.-K. Tao, and D. E. Johnson, 2004: Spectral retrieval of latent heating profiles from TRMM PR data. Part I: Development of a model-based algorithm. *J. Appl. Meteor.,* **43,** 1095–1113.

——, H. Sasaki, K. Okamoto, and T. Iguchi, 2006: Validation of rainfall estimates from the TRMM precipitation radar and Microwave Imager using a radiative transfer model: 1. Comparison of the version-5 and -6 products. *Geophys. Res. Lett.,* **33,** L13803, doi:10.1029/2006GL026350.

——, Y. N. Takayabu, W.-K. Tao, and C.-L. Shie, 2007: Spectral retrieval of latent heating profiles from TRMM PR data. Part II: Algorithm improvement and heating estimates over tropical ocean regions. *J. Appl. Meteor. Climatol.,* **46,** 1098–1124.

Simpson, J., R. F. Adler, and G. R. North, 1988: A proposed satellite Tropical Rainfall Measuring Mission (TRMM). *Bull. Amer. Meteor. Soc.,* **69,** 278–295.

——, C. Kummerow, W.-K. Tao, and R. F. Adler, 1996: On the Tropical Rainfall Measuring Mission (TRMM). *Meteor. Atmos. Phys.,* **60,** 19–36.

Soong, S.-T., and W.-K. Tao, 1980: Response of deep tropical cumulus clouds to mesoscale processes. *J. Atmos. Sci.,* **37,** 2016–2034.

Sui, C.-H., K.-M. Lau, W.-K. Tao, and J. Simpson, 1994: The tropical water and energy cycles in a cumulus ensemble model. Part I: Equilibrium climate. *J. Atmos. Sci.,* **51,** 711–728.

Takayabu, Y. N., 2002: Spectral representation of rain profiles and diurnal variations observed with TRMM PR over the equatorial area. *Geophys. Res. Lett.,* **29,** 1584, doi:10.1029/2001GL014113.

——, 2006: Rain-yield per flash calculated from TRMM PR and LIS data and its relationship to the contribution of tall convective rain. *Geophys. Res. Lett.,* **33,** L18705, doi:10.1029/2006GL027531.

Tao, W.-K., and J. Simpson, 1993: Goddard Cumulus Ensemble model. Part I: Model description. *Terr. Atmos. Oceanic Sci.,* **4,** 35–72.

——, S. Lang, J. Simpson, and R. Adler, 1993: Retrieval algorithms for estimating the vertical profiles of latent heat release: Their applications for TRMM. *J. Meteor. Soc. Japan,* **71,** 685–700.

——, ——, ——, W. Olson, D. Johnson, B. Ferrier, C. Kummerow, and R. Adler, 2000: Vertical profiles of latent heat release and their retrieval for TOGA COARE convective systems using a cloud resolving model, SSM/I, and ship-borne radar data. *J. Meteor. Soc. Japan,* **78,** 333–355.

——, and Coauthors, 2003: Microphysics, radiation and surface processes in the Goddard Cumulus Ensemble (GCE) model. *Meteor. Atmos. Phys.,* **82,** 97–137.

——, 2006: Retrieval of latent heating from TRMM measurements. *Bull. Amer. Meteor. Soc.,* **87,** 1555–1572.

Thompson, R. M. J., S. W. Payne, E. E. Recker, and R. J. Reed, 1979: Structure and properties of synoptic-scale wave disturbances in the intertropical convergence zone of the eastern Atlantic. *J. Atmos. Sci.,* **36,** 53–72.

Wang, Y., W.-K. Tao, and J. Simpson, 1996: The impact of ocean surface fluxes on a TOGA COARE cloud system. *Mon. Wea. Rev.,* **124,** 2753–2763.

Webster, P. J., and R. Lukas, 1992: TOGA COARE: The Coupled Ocean–Atmosphere Response Experiment. *Bull. Amer. Meteor. Soc.,* **73,** 1377–1416.

Yanai, M., and R. H. Johnson, 1993: Impacts of cumulus convection on thermodynamic fields. *The Representation of Cumulus Convection in Numerical Models, Meteor. Monogr.,* No. 46, Amer. Meteor. Soc., 39–62.

——, S. Esbensen, and J.-H. Chu, 1973: Determination of bulk properties of tropical cloud clusters from large-scale heat and moisture budgets. *J. Atmos. Sci.,* **30,** 611–627.

——, J.-H. Chu, T. E. Stark, and T. Nitta, 1976: Response of deep and shallow tropical maritime cumuli to large-scale processes. *J. Atmos. Sci.,* **33,** 976–991.

Yasunari, T., 1994: GEWEX-Related Asian Monsoon Experiment (GAME). *Adv. Space Res.,* **14,** 161–165.

Yuter, S. E., and R. A. Houze Jr., 1995: Three-dimensional kinematic and microphysical evolution of Florida cumulonimbus. Part II: Frequency distribution of vertical velocity, reflectivity, and differential reflectivity. *Mon. Wea. Rev.,* **123,** 1941–1963.

——, ——, E. A. Smith, T. T. Wilheit, and E. Zipser, 2005: Physical characterization of tropical oceanic convection observed in KWAJEX. *J. Appl. Meteor.,* **44,** 385–415.

Zeng, X., and Coauthors, 2007: Evaluating clouds in long-term cloud-resolving model simulations with observational data. *J. Atmos. Sci.,* **64,** 4153–4177.